Drop impact on thin film: mixing, thickness variations and ejections

J. Parmentier, V. Terrapon, and T. Gilet
Department of Aerospace & Mechanical Engineering, University of Liège, Belgium
(*jparmentier@uliege.be)

(Dated: February 24, 2026)

The impact of drops on a thin liquid film is a phenomenon encountered in industrial applications, but also of particular interest in nature. Examples include the growth of stalagmites in karstic caves, a case where the drop feeds the film with ions that will subsequently precipitate. The mixing upon impact, which is witnessed both in the film and in the ejections, remains poorly understood. In the case of stalagmites, this short-term mixing directly affects the ion distribution in the film between impacts. In this work we investigate the mixing and ejection processes occurring during the impact of a free-falling drop on a thin, horizontal film of miscible liquid. We perform laboratory experiments and record side and top views of high-speed movies of impacts in a range of parameters close to impacts observed on stalagmites in caves. We observe that several outcomes arise from these impacts depending on the initial film thickness and Weber number. We relate the geometry of the splashing crown growth to the four scenarios observed. Additionally, the post-impact mixing patterns and film thickness variations are analyzed through an original colorimetry-based technique. From there we infer the size of the stain and quantity of water left by the drop in the film, as well as the total volume ejected away during the impact.

I. INTRODUCTION

Drop impacts have been widely studied for the past decades [1, 2], partly because of their ubiquity in many industrial processes such as spray painting and cooling [3], microelectronics soldering [4], or crop spraying [5]. They also have multiple natural occurrences, e.g., the aeration of ocean surfaces [6], soil erosion [7–9], or the rain-induced foliar spreading of pathogens in crop fields [10–12]. The applicative context of this study is the growth of stalagmites in karstic caves, which are formed through accumulation of calcium ions brought in by the impacting drops, and their precipitation into calcite [13]. The precipitation occurs within a thin residual water film lying on top of the stalagmites. Degassing of carbon dioxide from this film toward the cave atmosphere governs the global kinetics of the chemical reactions at play [14]. At the same time, the film is drained away by gravity. Both the film and the ions in solution are progressively renewed by successive drop impacts.

The modulations of stalagmite growth can be witnessed in the successive laminae visible in longitudinal cuts. These laminae are expected to provide useful information for palaeoclimate reconstruction [9, 15–18], especially in regions where no other proxys such as sediments or ice cores are available. The inter- and intraseasonal variations of environmental parameters such as the partial pressure in carbon dioxide, the cave temperature or the soil coverage above the cave were shown to modify the average growth rate of the stalagmites on limited time periods [13, 19–21]. However, most models describing speleothem growth lack a characterization of the aerodynamics and hydrodynamics at play when drops impact stalagmites [13, 22, 23]. For example, the free fall of the drops yields a scattering of sometimes several centimeters in their impact point distribution. This dispersal was recently shown to strongly correlate to the average width of stalagmites related to one active stalactite [24]. Moreover, stalagmite growth models consider the liquid film lying on top of the stalagmite to be uniform in time and space [13], which may not always be appropriate as film thickness variability should have a direct effect on the ion distribution and precipitation. The distribution of ions following each impact results from the balance between the distribution of ions already in the film before the impact, the amount of ions brought by the drop in the film at each impact, and possibly the amount leaving the film due to splashing. In other words, the growth of stalagmites might be correlated to the mixing between the incoming drop and the film. However, to fully comprehend the possible influence of this mixing, it should be coupled with the other phenomena at play, namely, the filling and depletion dynamics of the film due to both the impacts and gravity-induced drainage, and the ion precipitation.

Owing to the sometimes very high cave ceilings, drops landing on stalagmites may reach impacting velocities up to 10 m/s [24], similarly to large raindrops [25]. However, by contrast with raindrops [26], the radius of the drops originating from stalactites is fairly constant and close to the capillary length, namely $r_\mathrm{d} \simeq 2.6\,\mathrm{mm}$ [24]. Given these size and speed, most drop impacts on stalagmites lead to splashing. In caves, drops having a fall as short as $30\,\mathrm{cm}$ would actually splash when impacting the underlying film, independently of its thickness [27]. On average, the film thickness δ ranges between a few tens and a few hundreds of micrometers [24], yielding the ratio $\delta/(2r_\mathrm{d})$ to be comprised between 10^{-3} and 10^{-1}.

A few studies already characterized drop impacts on thin liquid films for which $\delta/(2r_\mathrm{d}) \lesssim 10^{-1}$, as in caves. However, they focused mostly on the splash morphology [28–32], and more particularly on the splashing threshold [33, 34]. The influence of the fluid viscosity [30, 33–35] was also investigated, as well as the underlying surface roughness [33, 36], or the (im)miscibility between the drop and the film [37, 38]. Ersoy and Eslamian [39] further characterized the various physical processes at play that induce mixing between the drop and the film during the collision. However, several features of drop impacts on thin films have not been quantified yet, e.g., the proportion of the incoming drop volume which is ejected away in the splash droplets, or how much liquid coming from this drop would actually end up in the film after the impact. These quantities are necessary to better describe the hydrodynamics of drops impacting stalagmites and their possible influence on subsequent stalagmite growth. This knowledge could also be useful in other contexts, e.g., to rationalize some of the mechanisms of rain-induced pathogen dispersal in between plant leaves [11].

In this work we investigate the mixing and ejection processes as they would occur when drops impact stalagmites in caves. We therefore aim at studying drops with a large falling height, i.e., which are highly accelerated, impacting on horizontal, thin, miscible films. To do so, we perform laboratory experiments and record side and top views of high-speed movies of such impacts in a range of parameters close to actual cave values. We observe that several outcomes arise from these impacts depending on the initial film thickness, and have a strong influence on the final retraction phase of the crown formed during the impact and on the amount of liquid ejected at the same time. The retraction phase is further found to be responsible for the variability of the shape left by the drop in the film after the impact, and therefore on the mixing between the drop and the initial film. Image analysis is used to describe the geometry of the crown from the side. For the top view of the impacts, we use different dyes to color the drop and the film prior to the impact in order to identify the liquid coming from either one in our movies. Our conclusions regarding the mixing between the dyes would also be applicable to ions in the context of stalagmites. Post-impact ion distribution directly affects subsequent precipitation and hence, potentially, stalagmite growth.

II. MATERIALS AND METHODS

The following subsections describe our experiments of falling drops impacting on thin films with high velocity. More specifically, we first give an overview of the experimental setup (subsection II A), along with the corresponding parameters. We further describe the quantities measured in the high-speed movies of these impacting drops. We then explain how we measure the thickness of the films with precision. We also provide a short summary of the colorimetry-based algorithm used to analyze the experiments (subsection II B). We finally carry out a dimensional analysis in which we consider all the characteristic timescales at play and variables involved in the experiment (subsection II C). All the measured variables and fluid properties are summarized in Table II.

A. Laboratory measurements

1. *Experimental procedure*

The experimental setup is schematized in Fig. 1 (a). Water drops were released one at a time from a given height. They fell and impacted a film of miscible liquid at rest. The film of thickness δ laid on a horizontal solid surface of negligible roughness. Water has a density $\rho \simeq 1000\,\mathrm{kg\,m^{-3}}$, a surface tension $\gamma \simeq 70\,\mathrm{mN\,m^{-1}}$ and a kinematic viscosity $\nu \simeq 10^{-6}\,\mathrm{m^2\,s^{-1}}$ at room temperature ($20 \pm 2\,^{\circ}\mathrm{C}$). The drops were formed at the tip of a 2 mm diameter plastic connector (Cole-Parmer, polypropylene Masterflex adapter fitting), with a flow rate of $5\,\mathrm{\mu L\,min^{-1}}$ imposed by a syringe pump (WPI, AL-1000). The syringe pump operated until a drop was produced, then it was stopped during the video recording and data processing. The drop fall was protected from potential parasitic air currents by a 20 cm diameter rigid tube, which was sufficiently large to neglect the aerodynamic interaction of the falling drop with the tube. The impact position could however still vary by a few millimeters for large falling heights as the drops could interact with the vortices shed in their own wake [24]. High-speed movies of the impacts were recorded from the top using a Phantom Miro M110 color camera (6200 fps), and from the side with a Photron Fastcam Mini UX monochrome camera (4000 fps). In the top view, 1 cm corresponds to 125 px and the field of view is roughly $40 \times 40\,\mathrm{mm}$. In the side view, 1 cm corresponds to 230 px and the field of view is $55 \times 45\,\mathrm{mm}$. The top camera was inclined by a very small angle with the vertical ($5^{\circ} - 10^{\circ}$). A comparison between a few matching side and top view measurements of the radius of the cavity made by the crushing drop in the film ensured that this tilt angle did not significantly affect the top view lengths, hence no correction was applied.

The liquid film was dispensed onto a hydrophilic tape (Adhesive Research, ARflow 93210) fixed to an underlying stiff plate thanks to a sandwiched layer of double-sided, white tape. The hydrophilic tape has a thickness of $102\,\mu$m, a negligible roughness, and advancing and receding contact angles of 20° and $\lesssim 1^{\circ}$, respectively. The surface of the film corresponded roughly to a 40 mm side square. The film was carefully deposited with a syringe and spread out evenly by gently tilting the plate until the entire tape surface was wet. The average film thickness was varied between $65\,\mathrm{\mu m}$ and $500\,\mathrm{\mu m}$ by dispensing the corresponding liquid volume on the tape, and measured pointwise manually prior to the impact (see section II A 2).

The side movies were analyzed using image processing tools, which allowed to measure geometrical parameters related to the impacting drop and subsequent crown development, all listed hereafter and shown in Fig. 1 (b) i (see also Appendix Table II). The drop radius and velocity were measured in all the side movies. The drops all have the same radius $r_{\mathrm{d}} = 2.3 \pm 0.1\,\mathrm{mm}$. The falling height was varied between 50 cm and 4 m, leading impact velocities u_{d} to be comprised between $2.9\,\mathrm{m\,s^{-1}}$ and $6.6\,\mathrm{m\,s^{-1}}$. The measurements of u_{d} have a mean relative error of 3 % (i.e., the average of the errors made in each movie analysis). The crown inclination α, namely the angle made by the crown with the horizontal, varies between 50° and 105° during crown

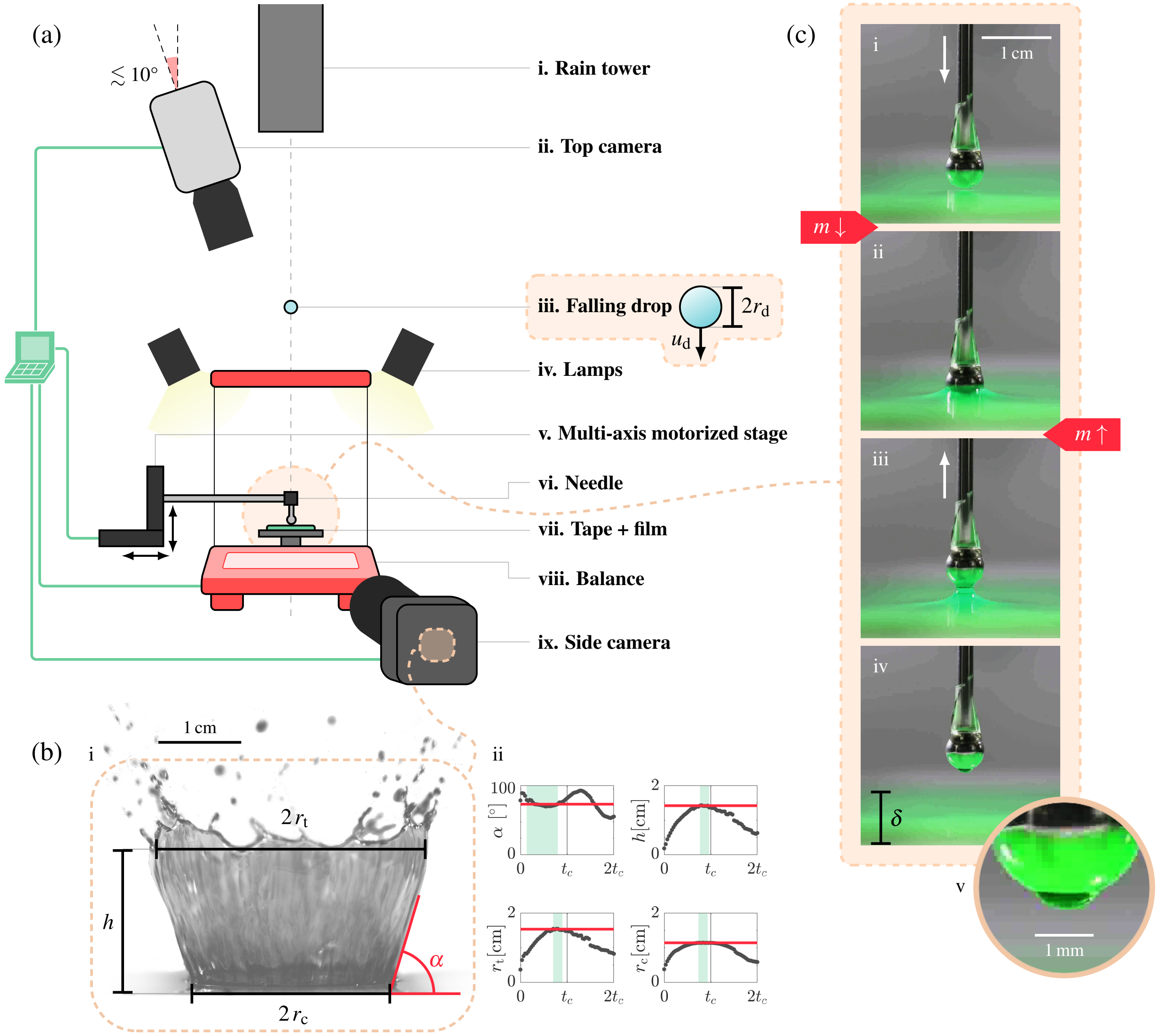

FIG. 1. Experimental methodology. (a) Experimental setup used to release droplets from a given height onto a thin underlying film, and record the impacts from both top and side views. i. Plastic tube in which the drops fall. ii. High-speed color camera used to record impacts from the top. iii. Falling droplet of radius r_d and impact velocity u_d, both measured from the side view (see (b)). iv. Four lamps placed in the corners of the balance. v. Stages used to displace the needle above the film, horizontally and vertically. The vertical stage is motorized and automated. vi-viii. Needle and balance used to take pointwise manual thickness measurements (see (c)) of the liquid film spread on a horizontal hydrophilic tape. ix. High-speed monochrome camera used to record impacts from the side. (b) i. Side-view geometrical measurements of the crown: crown height h, top radius r_t, cavity radius in the film r_c and inclination α. The drop schematic of (a) iii has a size corresponding to the actual drop that produced the crown shown in this case. ii. Four examples of raw data graphs of $\alpha(t)$, $h(t)$, $r_t(t)$ and $r_c(t)$, respectively, during a period of twice the capillary time t_c defined in Section II C (15 ms), for $\delta = 150\,\mu$m and $z = 1$ m. In each graph, the green area shows the portion on which measurements are averaged as described in the text, and the average is represented by the red line. (c) Needle with glued aluminum sphere used for measuring the local film thickness, entering (i-ii) and leaving (iii-iv) a green film of thickness $\delta = 170\,\mu$m. i. The needle and sphere right before the sphere touches water. ii. The meniscus formed when the sphere touches the film. This event produces a decrease in the mass read by the balance since a part of the film weight is supported by the needle. The needle is moved further downward and the mass increases once the sphere touches the bottom surface of the film. The needle is then moved upward. iii. The shape of the meniscus right before it separates from the sphere. iv. The droplet left on the sphere 4 s afterwards. v. A zoom on this droplet hanging on the bottom half of the aluminum sphere. Both appear green because of light reflections from the green film.

growth, with a relative error of 3 % on average for all the movies. The measurements correspond to the mean inclination from

2 ms to about 10 ms after the beginning of the impact for thicker films ($\delta \gtrsim 100\,\mu\mathrm{m}$). They were only taken up to 6 ms for thinner films to avoid taking measurements during the crown fragmentation (see Section III A). The measured ranges of crown maximum height h, top and bottom radii r_t and r_c are $h/r_\mathrm{d} \in [3\ ;\ 10]$, $r_\mathrm{t}/r_\mathrm{d} \in [5\ ;\ 9]$ and $r_\mathrm{c}/r_\mathrm{d} \in [4\ ;\ 8]$. These variables are independent: they cannot be related by a simple geometrical relation as the curvature of the crown wall changes in response to the film thickness, i.e., for a given $r_\mathrm{t}/r_\mathrm{c}$ ratio there might be different values of α and h. The measurements of h, r_t and r_c all correspond to the average of the 5 largest values measured during the crown growth. The average relative errors are respectively of 12 % (h), 11 % (r_t) and 8 % (r_c). The error made when measuring the first two variables is due to the unstable rim, which altered the detection of the crown/air interface in the video. Examples of raw data obtained for $\alpha(t)$, $h(t)$, $r_\mathrm{t}(t)$ and $r_\mathrm{c}(t)$ are shown in Fig. 1 (b) ii during the beginning of the impact, i.e., during the crown growth ($t \lesssim t_\mathrm{c}$) and beginning of the retraction ($t > t_\mathrm{c}$), with t_c the capillary time defined in Section III. For falling heights smaller than 1 m, the maximum length j reached by the Worthington jet emitted at the end of the retraction is such that $j/r_\mathrm{d} \in [3\ ;\ 10]$, with a relative error of 15 %. This length was taken in the last frame before the first secondary droplet pinches off. The large error in j comes from the possible inclination of the jet (see, e.g., Fig. 6 (c) iii) which might occur in a plane orthogonal to the field of view.

2. *Manual film thickness measurements*

To estimate the film thickness, we used the average value of mechanical pointwise measurements taken in 3 to 5 spots separated by 1-2 cm, close to the center of the film. As depicted in Fig. 1 (a), measurements were performed using a Ohaus Pioneer X balance (precision of 0.1 mg) and a needle attached to a high-precision motorized translation stage (smallest displacement of 0.1 µm). The balance was protected from parasitic air currents by vertical glass windows. Two other translation stages permitted to move the needle horizontally and take measurements at any point of the film. A Thorlabs Kinesis stepper actuator controlled via an automated routine allowed to displace the needle vertically by discrete steps. At each step the needle was moved with a velocity of $250\,\mu\mathrm{m\,s^{-1}}$, then it remained still until the next instruction (acceleration/deceleration of $1\,\mathrm{mm\,s^{-2}}$). Although the displacement of the stage was almost instantaneous, the needle position and the mass on the balance were recorded only about every second, owing to the limited acquisition frequency of the balance. A small aluminum sphere was glued to the tip of the hollow needle in order to avoid capillary rise (Fig. 1 (c)). Once this sphere reached the water free surface, a small meniscus appeared, which translated into a small decrease in the mass read by the balance (Fig. 1 (c) i-ii). As the needle was moved further down, the sphere ended up touching the solid surface (tape) beneath the water film, increasing this time the mass read by the balance (Fig. 1 (c) ii-iii). Both these events allowed to obtain the difference in position of the needle and therefore the height of the water film at a given horizontal location. During this procedure, steps of 1 µm were used before the sphere could touch the water free surface. Then the step size was increased to 15 µm such that the measurement time did not exceed 1-2 min. As soon as the sphere touched the solid surface beneath the film, the needle was moved upward once then downward again, this time by steps of 1 µm. On average, the standard deviation of the manual film thickness measurements is 3 µm. The relative error ranges from 3 % for thinner films ($\lesssim 100\,\mu\mathrm{m}$), to 1 % for larger ones ($\gtrsim 250\,\mu\mathrm{m}$).

A small amount of liquid (volume corresponding to a sphere of radius $300 \pm 20\,\mu\mathrm{m}$) remained on the tip once the sphere had come out of the water because of this meniscus, as seen in Fig. 1 (c) iv-v. This droplet usually evaporated between two successive measurements. When some liquid was spotted on the needle tip, it was wiped off carefully.

B. Colorimetry measurement

1. *Film thickness and concentration profiles*

To observe the mixing between the drop and the film after impact as well as the potential variations in film thickness, we have developed a colorimetry-based algorithm to analyze top view images of the experiments approximately 1 s post impact. For this purpose, we combined two food dyes to color the drop and the film differently: red (Azorubine, E122) and green (corresponding to 3/4 of yellow, Tartrazine, E102, and 1/4 of FCF blue, E133). When bought, these commercial dyes were already in solution, with a fixed but unknown concentration. We subsequently diluted them in DI water, with proportion (volume fraction) p_r and p_g for the red and green dyes, respectively. The colorimetry measurement is described in detail in Appendix B 1. It relies on the assumption (checked in Appendix B 2) that in a given optical and lighting set, there is a bijective relation between the (R,G,B) on-screen color triplets and particular values of the thickness and concentrations of dyes in the film. This bijection can be formalized by considering the Beer-Lambert absorption of the light beam in the different media crossed from the light source to the camera, as well as the Fresnel reflection/refraction at the interfaces between these media. In this manner each color channel may be independently related to the film thickness and dye concentrations. The equations obtained are further approximated by quadratic relations. To estimate at best the coefficients therein, we first used calibration pictures for which we imposed δ, p_r and p_g and recorded the corresponding RGB pictures. A total of 175 water films were used, with thickness ranging in the same interval as in our experiments (and thus as in caves). Both the red and green proportions were varied between 0 and 0.075 (see

Supplementary Material). These values were empirically chosen in order to yield distinguishable on-screen variations in the given thickness range. Calculations were not performed for each pixel but rather in 0.8 mm (≈ 10 px) side square cells, where the median value of each color channel was computed. A 4 mm (≈ 50 px) wide stripe was also cut around the pictures to avoid seeing the physical edge of the tape, leaving a field of view of 32 mm × 32 mm (40 × 40 cells) to analyze.

Once the calibration was performed, from every given (R,G,B) triplet, we could infer the film thickness and red and green dye composition in a thin film of arbitrary local composition. An example of the shape observed about 1 s after the impact is shown in Fig. 2 (a), in the case of a drop falling from 2 m on a film of initial thickness 103 ± 1 µm. In the actual experiments, we were interested in computing the post-impact film thickness δ and the proportion of liquid coming from the drop, which were *a priori* unknown. In order to obtain them, red and green dyes were mixed in equal proportion $p_{r,\mathrm{d}} = p_g = 0.05$ in the initial drop, while only green dye in the same concentration ($p_g = 0.05$) was present in the initial film. Therefore, the green dye concentration remained constant in time and space, independently of the mixing of the drop and the film, while the red dye concentration revealed the parcels of fluid that originated from the initial drop. Hence, we are left with two independent variables δ and p_r to be determined. We change variables and define the partial film thicknesses in red and green respectively as $\delta_r = p_r\delta$ and $\delta_g = p_g\delta$. Since there are only two independent variables, the relation between the (R,G,B) channels and the partial thicknesses (δ_r,δ_g) gives an overdetermined system that is solved in the least square sense. Although neglecting the blue channel would yield a system that is not overdetermined, the procedure appeared more robust when the blue channel was considered. From the measurement of δ_g given by the analysis of the (R,G,B) values in every cell, we deduced the film thickness as $\delta = \delta_g/p_g$. We further inferred the red dye proportion as $p_r = \delta_r/\delta$. Examples of measurements obtained with this algorithm are shown in Fig. 2 (b) and (c). The diagram of Fig. 2 (b) shows the red dye proportion left in the film after the impact from the picture of Fig. 2 (a), compared to the initial red proportion in the drop $p_{r,\mathrm{d}}$. The film thickness variation $\delta' - \delta$ between after (δ') and before (δ) the impact is shown in Fig. 2 (c).

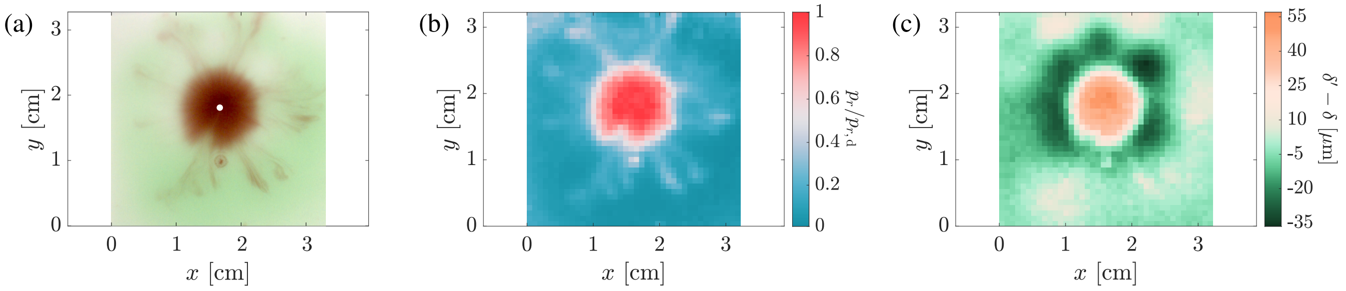

FIG. 2. Example of an impact experiment (a) and measurements obtained with the colorimetry-based algorithm (b-c): (a) Top view picture of the spot left by the drop in the film about 1 s after the impact. The initial film thickness was $\delta = 103$ µm and the drop had a fall of 2 m. The white dot in the center of the photograph corresponds to the impact point. (b) Red dye proportion left in the film after the impact, normalized by the proportion in the drop, $p_r/p_{r,\mathrm{d}}$. (c) Film thickness difference between after and before the drop impact on the film, $\delta' - \delta$ (in µm).

2. *Comparison between manual and colorimetry measurements of the film thickness*

Pointwise manual film thickness measurements were performed for the calibration process. They were also made before the impacts to ensure the film thickness uniformity. Special care was needed to level the balance, since a slight tilt angle of only 0.1° from the horizontal would yield a 50 µm difference between two points located 30 mm apart in the film. The levelling was achieved by manually adjusting the balance legs in response to any film thickness variation larger than 5 µm that was potentially observed between two points in the film. Pointwise thickness measurements further allowed getting a rough estimation of the average thickness of the deposited film. This estimation is useful for the colorimetry measurement which is based on Newton-Raphson iterative method and therefore requires an initial guess. Knowing the mean thickness of the film also allowed verifying the results provided by this algorithm. In Figs 3 (b) and (c) the results computed by the algorithm are represented for a given calibration film of proportions $p_{r,\mathrm{m}} = 2.5\,\%$ and $p_{g,\mathrm{m}} = 5\,\%$, shown in Fig. 3 (a). The manually measured thickness δ_m for this film was 135.8 ± 2.1 µm (average ± standard deviation over several successive measurements on the same film, taken at different locations). The film thickness and red proportion obtained with the colorimetry measurement are respectively $\delta_\mathrm{c} = 133.1 \pm 1.2$ µm and $p_{r,c} = 2.24 \pm 0.01\,\%$ (average ± standard deviation over the 40 × 40 cells of the picture). In other terms, a relative error of 2 % is made on the average film thickness and of 10 % on the average dye proportion in this case.

Additionally, in Fig. 4 the film thickness computed using the colorimetry measurement and spatially averaged, $\overline{\delta_\mathrm{c}}$, is plotted against the average manual film thickness measurement, $\overline{\delta_\mathrm{m}}$, for all the experiments using the pictures taken ante impact. The

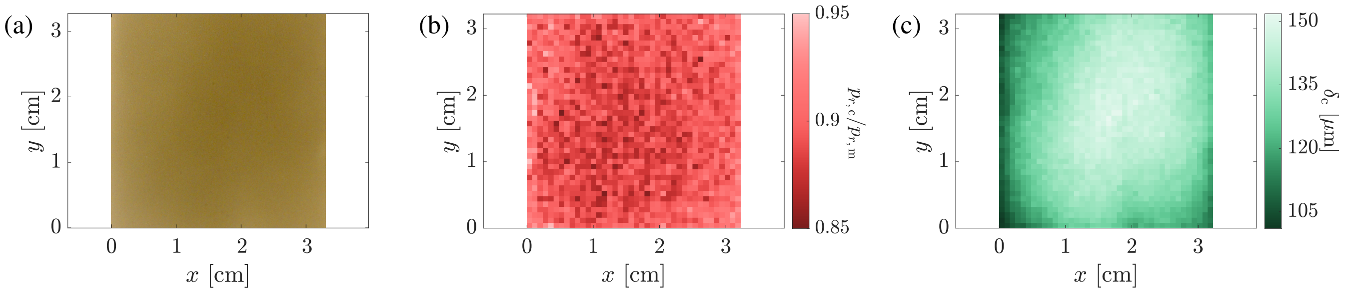

FIG. 3. Colorimetry calculation ($\cdot_c$) of the thickness and red dye proportion of an arbitrary calibration film: (a) Initial photograph taken with the Phantom Miro M110 high-speed camera. (b) Red proportion $p_{r,\mathrm{c}}$ computed at each point in the frame of (a), divided by the actual proportion $p_{r,\mathrm{m}} = 2.5\,\%$. (c) Thickness δ_c computed at each point of (a). Green dye proportion was set in every point to $p_g = 5$ %.

coefficient of determination obtained by linear regression is 0.91. Markers in the graph go from green to red as they get further away from the bisector line. The upper left inset of the graph shows a histogram detailing the number of experiments as a function of the relative error between the average manual and colorimetry measurements, $|\overline{\delta_\mathrm{m}} - \overline{\delta_\mathrm{c}}|/\overline{\delta_\mathrm{m}}$. About 65 % of the total number of experiments have a relative error smaller than 10 %, and 92 % of the experiments have a relative error smaller than 20 %. The lower right inset of Fig. 4 (a) shows the coefficient of variation (c.v.) of δ_c in space (i.e., for different cells of the same film), as a function of the corresponding average film thickness $\overline{\delta_\mathrm{m}}$. Because it is computed in every point of the picture, the c.v. is a measure of the spatial heterogeneity of the film thickness. The median (2.1 %) and interquartile interval ([1.1 ; 3.6] %) of the c.v. distribution for all the experiments are represented respectively by a green horizontal line and a shaded area in the back of the inset. The c.v. of δ_c thus seems equivalent to the error made when measuring the film thickness manually before the impact (ranging between 1 and 3 %). Similarly to the colorimetry measurement, the error on δ_m should thus mostly come from the heterogeneity of the film rather than from the measuring technique itself.

Because in reality the film is simply a very flat puddle, it is not surprising to find the same order of magnitude in the errors induced by the spatial heterogeneity obtained with the two methods. The c.v. is typically higher at smaller δ as it is more difficult to spread a large puddle of very low thickness, even on a hydrophilic substrate. The edges of the film therefore appear whiter on screen since there is less liquid, yielding an increased inhomogeneity of the film in the zone observed during the impact. In some cases this error can be large, as illustrated in Fig. 4 (b). In each of them, a square indicates the margin that was removed for the calculation so as not to see any edge of the tape below the film. Nevertheless, the thickness gradient seems visible in picture i, which translates in a average colorimetry thickness $\overline{\delta_\mathrm{c}} = 66.3\,\mu\mathrm{m}$ smaller than $\overline{\delta_\mathrm{m}} = 88\,\mu\mathrm{m}$. Therefore, when taking the whole picture into account in the calculation of $\overline{\delta_\mathrm{c}}$, a large difference between $\overline{\delta_\mathrm{m}}$ and $\overline{\delta_\mathrm{c}}$ appears but this error does not come from the evaluation of the thickness by the algorithm. In Fig. 4 (b) ii the thickness is correctly estimated as there is only an error of 2 % on the average value. Moreover, we cannot see the edge of the tape in the computation zone in the photograph. Overall, the errors mostly come from the puddle physical edge which might still appear in the pictures ($\overline{\delta_\mathrm{c}} \lesssim \overline{\delta_\mathrm{m}}$ in 70 % of the cases), but measurements may also be sensitive to tiny differences in the lighting setup or to the positioning of the camera, i.e., elements that had to be put back in place each day the experiment was carried out. In Fig. 4 (b) iii we observe an error of 6 % between the two spatially averaged thickness values, but this time $\overline{\delta_\mathrm{c}}$ is larger than $\overline{\delta_\mathrm{m}}$ due to such effects. The measurements from subsection IV B 1 are based on integration over a smaller region, hence such spatially dependent effects on the edges should not affect the results.

C. Dimensional analysis

In the considered configuration, the impacting drop first crushes on the film for a time scaling as the impact time, defined as $t_\mathrm{i} = 2r_\mathrm{d}/u_\mathrm{d} \lesssim 1\,\mathrm{ms}$. The radially spreading crown formed upon impact [2] has a lifetime of the order of the capillary time defined as $t_\mathrm{c} = \sqrt{4\rho r_\mathrm{d}^3/(3\gamma)} \simeq 15\,\mathrm{ms}$. This timescale is also characteristic of the lifetime of liquid sheets expelled into the air from droplets impacting on poles or close to solid edges [11, 40]. A viscous boundary layer is formed along the bottom wall as the film is pushed by the impacting drop. It diffuses through the entire film thickness in a timescale of the order of $t_\nu = \delta^2/\nu$. For the film thicknesses considered here (i.e., from 65 µm to 500 µm), this time ranges from 5 ms to 280 ms. The time of viscous diffusion over a distance equivalent to the drop radius is about $t_{\nu,\mathrm{d}} = r_\mathrm{d}^2/\nu \simeq 6\,\mathrm{s}$. Finally, molecular diffusion also has a role after the impact but occurs at a much larger timescale than the other phenomena at play. When considering sub-nanometer particles and ions with a diffusion coefficient $D \sim 10^{-9}\mathrm{m}^2\,\mathrm{s}^{-1}$, the vertical diffusion in a 100 µm thick film would take a time $t_\downarrow = \delta^2/D$

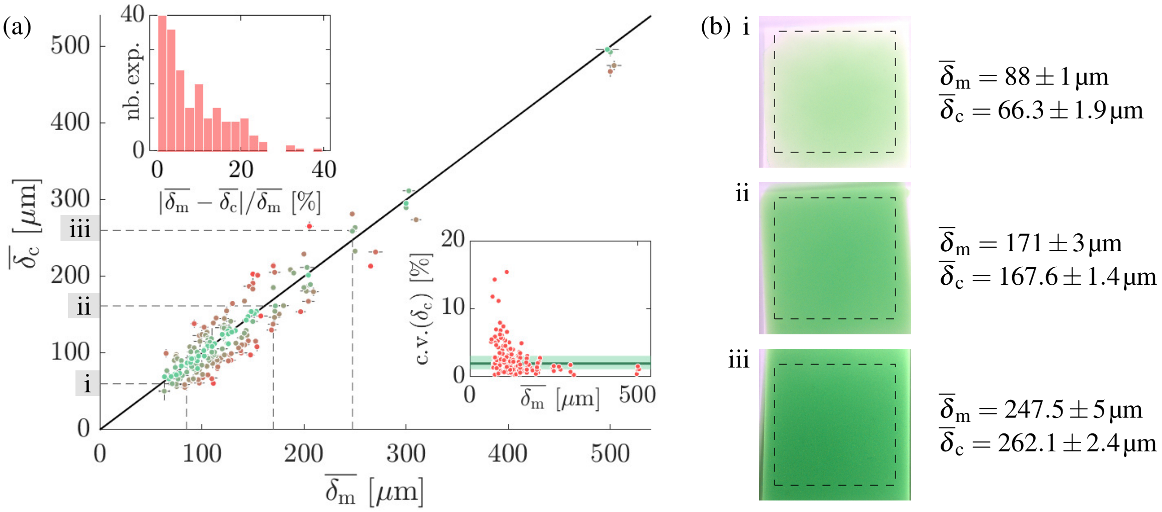

FIG. 4. (a) Parity plot between spatially-averaged film thickness $\overline{\delta_{\mathrm{c}}}$ computed from colorimetry measurements and corresponding film thickness manually measured and averaged, $\overline{\delta_{\mathrm{m}}}$, prior to the impact. Symbol color is greener (redder) for markers located closer to (further away from) the axes bisector. The left inset of the graph in (a) shows a histogram representing the number of experiments per range of relative error between manual and numerical measurements, $|\overline{\delta_{\mathrm{m}}} - \overline{\delta_{\mathrm{c}}}|/\overline{\delta_{\mathrm{m}}}$. The bins are 2 % wide. The second inset in (a) shows the coefficient of variation (c.v.) of δ_{c}, i.e., over different cells of the same film, as a function of $\overline{\delta_{\mathrm{m}}}$. The c.v. can be seen as a measure of the spatial heterogeneity of the film, and therefore as a characteristic error bar on $\overline{\delta_{\mathrm{m}}}$. The shaded area in this inset shows the interquartile range and the green horizontal line the median of the c.v. of δ_{c}. (b) Examples of colorimetry and manual measurements, sometimes leading to larger errors in the average film thickness estimation because of, e.g., the visibility of the puddle edge (see i), with correspondence in the graph from (a).

of about 10 s to homogenize the concentration over the entire film height. To diffuse such particles horizontally over a few millimeters, the characteristic timescale $t_{\rightarrow} = r_{\mathrm{d}}^2/D$ would be of the order of 90 min.

The impacts involve seven quantities (r_{d}, u_{d}, ρ, ν, γ, D and δ) that may all be expressed in terms of mass, length and time units. Hence, four nondimensional numbers govern the impacts and may be defined by comparing the characteristic timescales. First, the ratio $(t_{\mathrm{c}}/t_{\mathrm{i}})^2$ gives the Weber number defined as $\mathrm{We} = 2\rho r_{\mathrm{d}} u_{\mathrm{d}}^2/\gamma$. It compares the inertia of the drop to its surface tension and ranges in [525 ; 2750] in our experiments, as seen in the phase diagram of Fig. 5. The measurement errors made when evaluating r_{d} and u_{d} give a mean relative error of 9 % when calculating We. Second, the ratio $t_{\mathrm{c}}/t_{\nu,\mathrm{d}}$ leads to the Ohnesorge number which indicates how much viscosity modifies the balance of inertia and surface tension at drop scale, $\mathrm{Oh} = \nu\sqrt{\rho/(2\gamma r_{\mathrm{d}})}$. It takes a constant value of $1.7 \cdot 10^{-3}$ with a relative error of 2 %. A third ratio $\sqrt{t_\nu/t_{\mathrm{c}}}$ yields the dimensionless number $\delta^\star = \delta/\sqrt{\nu t_{\mathrm{c}}}$, which is a normalization of the film thickness by the thickness reached by the boundary layer in the film over the capillary timescale. A unit value for $\delta^\star$ corresponds to $\delta = 115.3\,\mu\mathrm{m}$. As also shown in Fig. 5, $\delta^\star \in [0.6 ; 4.3]$ with a relative error of 6 %. Additionally, the Péclet number Pe may be defined to compare the molecular diffusion and convection timescales. The convection timescale is here chosen as the timescale over which the impact-induced convection is damped, i.e. the viscous diffusion time, so $\mathrm{Pe} = t_{\downarrow}/t_\nu = \nu/D \sim 10^3$ and molecular diffusion can be neglected during the first seconds after impact, which are fully dominated by convection.

As $\mathrm{We} \gg 1$ and $t_\nu/t_{\mathrm{i}} \gg 1$ for all our impacts, the capillary and diffusive timescales are much larger than the impact time. Hence, while inertia dominates the first stages of the impact, capillary and viscous forces should only compete in the later crown development. Even higher We values could be observed in situ as cave ceilings are sometimes located up to several tens of meters above the ground [13]. Droplets in caves having falling heights going from 5 cm to 50 m would yield $\mathrm{We} \in [70 ; 7000]$ and Oh of about $2 \cdot 10^{-3}$ at a temperature of 12 °C [41], which are close to the experimental conditions of our impacts. The film thickness ranging from 50 µm to 500 µm would lead $\delta^\star$ values to be comprised between 0.4 and 4, i.e., a very similar range to ours. The particles found in the residual water film covering stalagmites, e.g., calcium ions and carbon dioxide, have diffusion coefficients of the same order as the dye molecules in our experiment, such that $\mathrm{Pe} \gg 1$ in caves as well. During the impact, convective transport is therefore much more effective than molecular diffusion. For impacts of actual stalagmites, molecular diffusion would play a significant role at a timescale comparable to those of ion precipitation and gravity-driven drainage, which are out of the scope of this study.

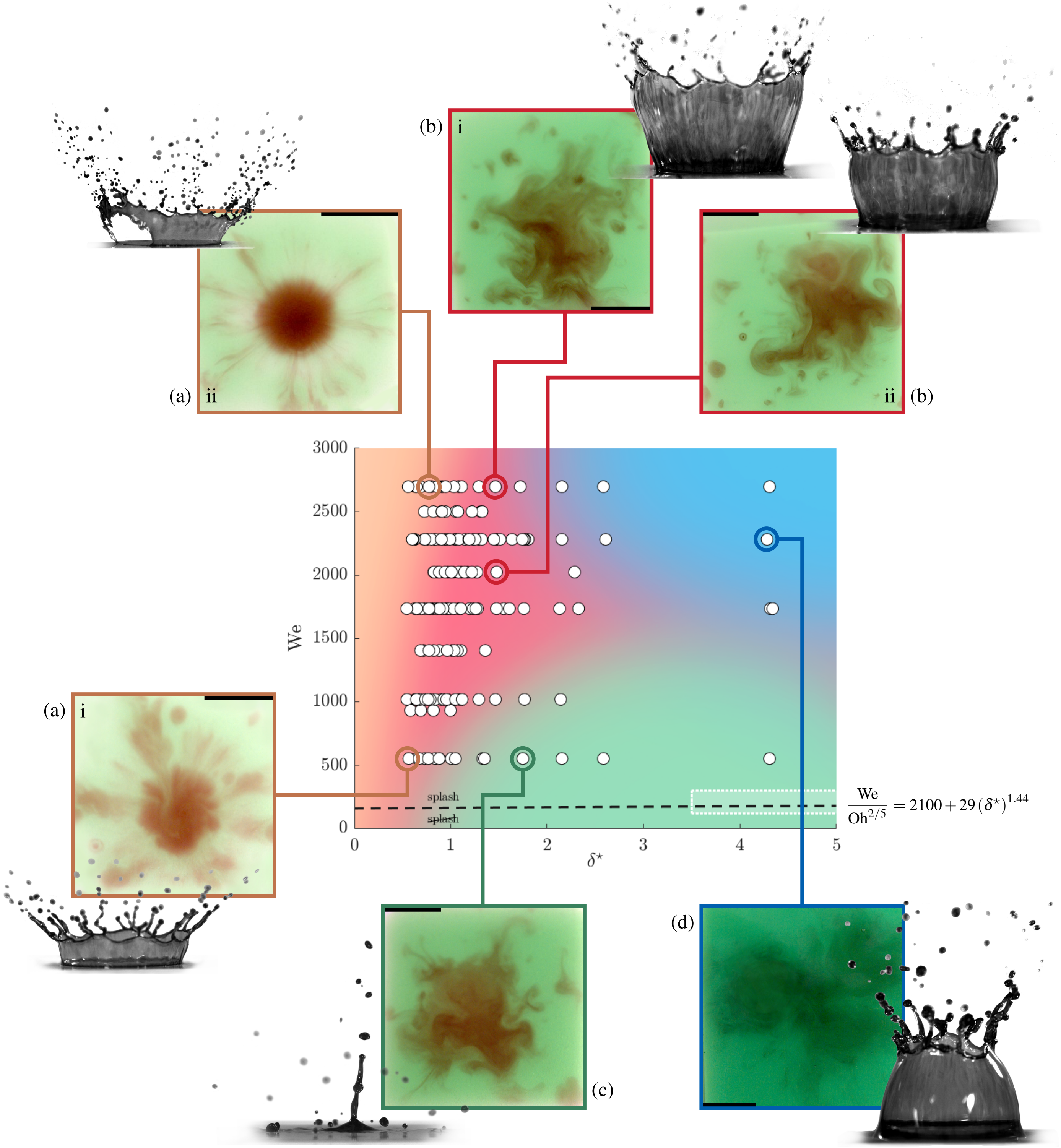

FIG. 5. Phase diagram ($\delta^\star$, We) of the reported experiments and correspondence with the various scenarios discussed in Sec. III. For each, the monochrome side view shows the typical shape of the crown during impact, while the color top view shows the post-impact mixing pattern. (a) Very thin film ($\delta^\star < 1$), crown fragmentation and circular red spot: i. Low We ($\delta^\star = 0.57$, $\text{We} = 525$), ii. High We ($\delta^\star = 0.61$, $\text{We} = 2740$). (b) Intermediate regime ($\delta^\star \gtrsim 1$), crown retraction and random-like mixing pattern: i. High We ($\delta^\star = 1.31$, $\text{We} = 2740$), ii. Intermediate We ($\delta^\star = 1.31$, $\text{We} = 1675$). (c) Thick film ($\delta^\star \gtrsim 1.75$), low We: post-impact central jet protrusion ($\delta^\star = 1.81$, $\text{We} = 525$). (d) Thick film ($\delta^\star \gtrsim 1.75$), high We: crown folding ($\delta^\star = 4.37$, $\text{We} = 2250$). Background color grading of the central graph indicates that scenario transitions are continuous. The shaded area in the bottom right of the central plot represents the range of values covered in Ersoy and Eslamian [39]. The dashed black line show the splashing criterion developed by Cossali et al. [33]: $\text{We}/\text{Oh}^{2/5} = 2100 + 29\,(\delta^\star)^{1.44}$. The scale bars are 1 cm.

III. OBSERVATIONS AND PHENOMENOLOGY

Drop impact on a thin film bridges the gap between two limits: impacts on a dry wall and on a deep liquid reservoir. For impacts on dry wall, the liquid left by the drop recoils at the end of the movement. It forms an almost circular liquid puddle surrounded by short tails reminiscent of the fingering occurring during the impact [11]. Drop collision with a dry wall has been extensively studied, most authors focusing on the splashing threshold [42] or the maximum spreading radius reached by the impacting drop [43–45]. These quantities change for instance in response to substrate roughness [46], surface wettability and properties [47, 48], inclination [49] or curvature [50], parameters that vary much in nature. In the other limit, the drop impinges on a deep pool, i.e., of a depth δ that is at least of the order of the drop radius r_{d}. This regime can be observed for some stalagmites with a concave summit that forms a small pool filled with water [24]. The impact produces an upward-moving cylindrical liquid sheet, the crown, due to the kinematic discontinuity between the crushing drop and the formerly resting liquid pool [1, 2]. Instabilities in the rim of this crown formed at impact are responsible for the appearance of small ligaments which subsequently destabilize into secondary droplets [29, 30, 33]. For more viscous fluids the droplets ejected from the crown typically appear in the later stages of the impact or may not be observed at all [30, 34]. As the crown grows radially and encounters new fluid from the pool, it thickens progressively and its height increases [28]. The diameter of the ligaments and subsequent ejected droplets grows accordingly [11, 30]. The crown also surrounds a hemispherical cavity growing in the liquid pool, which eventually recedes as the crown breaks up. Its typical maximum size is of the order of a few centimeters for our drop size [51, 52]. A Worthington jet may protrude from the center of this crater and pinch off into several droplets [29, 53, 54]. Because of the strong surface and bulk perturbations caused by this dynamics, the mixing between the drop and the liquid pool is pretty effective. Once the fluid is back to rest, mixing is usually completed through molecular diffusion in all directions [39]. Furthermore, most secondary droplets fall back into the pool as they typically do not have enough horizontal momentum to travel more than a few centimeters away from the impact point (i.e., if such deep pool conditions were observed in caves, the ejected droplets would likely impact on the stalagmite again) [54].

Most stalagmites are covered by a film of water that is very thin in comparison with the impacting drop size [24]. In a similar manner to drop impact on a deep pool [1, 51, 55, 56], this type of impact leads to the formation of an ascending crown, yet presenting a smaller inclination. The crown wall surrounds a cavity of thickness smaller than that of the initial film. Even in the early expansion stages, the rim on the perimeter of the crown also turns into tiny ligaments that subsequently break into secondary droplets due to the high kinetic energy of the impacting drop [27]. Cossali et al. [28] provided a detailed description of the crown radius, height and rim thickness evolution with time as well as the number of ligaments and droplets ejected from the rim, in a range corresponding to $(\delta^\star, \mathrm{We}) \in [11;43] \times [300;840]$, with $\mathrm{Oh} = 1.9 \cdot 10^{-3}$. Fedorchenko and Wang [35] derived a model describing the velocity of cavity submergence, central jet formation and crown ejection in impacts on film sufficiently thick to produce a Worthington jet. Wang and Chen [27] also explored the influence of viscosity on the impact outcome by varying the Ohnesorge number between 0.02 and 0.1 for $(\delta^\star, \mathrm{We}) \in [1.6;16.8] \times [380;3000]$. However, the range corresponding to thin films like those found on stalagmites has not been explored yet.

Our experiments reveal four main impact scenarios in different regions of the $(\delta^\star, \mathrm{We})$ diagram of Fig. 5, which are denoted scenarios A to D and described in the corresponding sections hereafter. They fall within the splashing limit derived by Cossali et at. [33] as a function of We, Oh and $\delta^\star$: $\mathrm{We}/\mathrm{Oh}^{2/5} = 2100 + 29\,(\delta^\star)^{1.44}$. In scenario A (orange), for all We and very thin films ($\delta^\star < 1$), the crown tears apart before the end of its expansion. In contrast, in scenario B (red) for which $\delta^\star \gtrsim 1$ for all We, the crown reaches a maximum height and retracts without breaking up. Scenarios C (green) and D (blue) correspond to large film thicknesses, for which $\delta^\star \gtrsim 2$. Scenario C is mostly characterized by the appearance of a central jet after the impact at low We. In scenario D, at high We, the crown retracts by folding upon itself. These scenarios thus differ in terms of the shape of the crown and related geometrical parameters, such as the inclination [35], and the later breaking and retraction of the crown [57]. Accordingly, the observed stains left by the drops in the films present various shapes and patterns. The total volume of liquid ejected during impact is consequently also directly affected by We and $\delta^\star$. The transitions between the various scenarios are not of first order though but rather continuous. This is illustrated by a color gradient in the phase diagram at the center of Fig. 5, while examples of typical impact sequences for various $\delta^\star$ and We are shown in Fig. 6 (a-d). Each subfigure in Fig. 6 shows frames (i-iii) taken from matching high-speed visualizations of the impacts from both side (in monochrome) and top views (in color). Each combination (a-d) of top and side views of one particular impact shows similar features (e.g., the crown growth), but due to the difference in impact dynamics, from one subfigure (a-d) to the other the corresponding instants shown are not the same. The last top view picture (iv) corresponds to the convection-induced mixing pattern. It is obtained at about 1 s (or equivalently $65\,t_{\mathrm{c}}$) after impact, i.e., when convection flows have vanished while molecular diffusion has not had the time to smooth horizontal concentration gradients yet. Noteworthy features of these impact scenarios are reported in Fig. 5 (a-d) as well.

A. Crown fragmentation

Crown fragmentation is observed for very thin films, i.e., such that $\delta^\star < 1$, and mostly for strong impacts, at $\mathrm{We} \gtrsim 1000$. This phenomenon was also observed by Wang and Chen [27], who reported crown wall fragmentation for $\delta^\star = 1.63$, $\mathrm{We} = 2010$

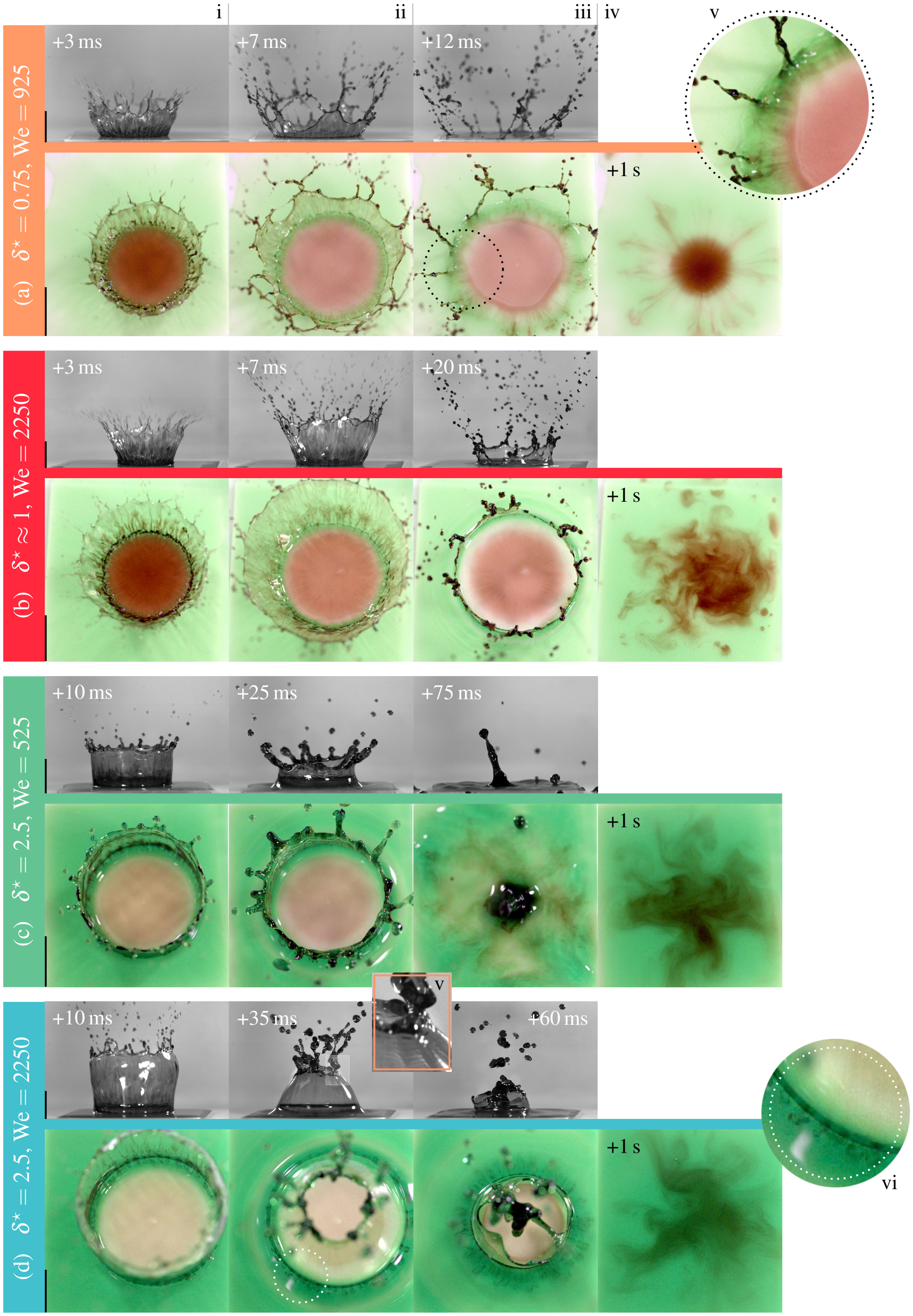

FIG. 6. Side (monochrome, upper pictures, *s*) and top (color, bottom pictures, *t*) views of the impact sequences described in Sec. III. For (a-d), i. shows the crown growth (*st*) and iv. the convection-induced mixing pattern (*t*). (a) Very thin film ($\delta^\star < 1$), intermediate We: ii. Crown break-up into ligaments (*st*), iii. Ligament fragmentation (*st*), v. Fingering-like pattern in the film (*t*). (b) Transitional regime ($\delta^\star \approx 1$), high We: ii. Crown maximum extension (*st*), iii. Retraction (*st*). (c) Thick film ($\delta^\star > 1$), low We: ii. Crown decline (*st*), iii. Post-impact central jet formation (*st*). (d) Thick film ($\delta^\star > 1$), high We: ii-iii. Crown folding (*st*), v. Crown capillary waves (*s*), vi. Fingering in the film (*t*). The scale bars are 1 cm. Videos corresponding to the pictures shown are available in Supplementary Material.

and Oh $= 0.04$ in water-glycerol solutions. The impact time, viscous diffusion time and capillary time are arranged as follows: $t_\mathrm{i} < t_\nu < t_\mathrm{c}$. In other words, the beginning of the impact is dominated by inertia as it is typically the case at high We [40, 51]. The crown expansion is decelerated primarily by viscous dissipation in the film, which considerably slows down the outward motion of the crown basis while the crown top keeps expanding thanks to its inertia. This translates into a very thin and inclined crown wall formed at impact (Fig. 6 (a) i), which becomes unstable and breaks into several thin sheets before it even starts to retract toward the center in response to capillary forces (Fig. 6 (a) ii) [27, 35]. The maximum extension reached by the rim at the top is larger than the radius of the cavity formed in the film, i.e., $r_\mathrm{t}/r_\mathrm{c} > 1$. The liquid sheet almost immediately ($\lesssim 5\,\mathrm{ms}$) turns into ligaments that subsequently break to form more secondary droplets (Fig. 6 (a) iii), in a very similar manner to when an impacting drop spreads beyond the edge of a solid substrate, and subsequently fragments. [11, 40]. Compared to the other regimes, the ligaments and droplets ejected both during the growth and fragmentation phases are small and fast [57] (radii and velocities of the order of $[0.07\ ;\ 0.25]r_\mathrm{d}$ and $[0.3\ ;\ 0.8]u_\mathrm{d}$, respectively). At the same time, we observe red filaments propagating throughout the crown (Fig. 6 (a) i-ii). Although it is obvious that these filaments come mostly from the drop because of their color, no quantitative measurement of the mixing level between the drop and the film during crown growth could be inferred from such visualizations.

Radial convective retraction followed by expansion strokes is usually observed after an impact in a deep pool or on a dry wall [1, 2, 58]. However, in this case the liquid left from the crushing drop in the film only seems to retract without expanding much afterwards, except for late molecular diffusion-driven expansion. The viscous forces should indeed rapidly dissipate any remaining kinetic energy left following the impact, once the crown has torn apart. Hence, the mixing pattern right after impact in this case simply corresponds to a circular, very red spot. This spot is surrounded by a whiter zone that seems to indicate some depletion in the film directly around the impacted area, possibly because of the absence of rapid expansion and retraction strokes (Figs 5 (a) ii and 6 (a) iv). Outside of this region, the film appears to be left unaffected by the passage of the crown, except for a few thin radial tails. These tails come from the coalescence of the last ligaments breaking at the end of the crown fragmentation with the underlying film. Even though the coloration of the spot left by the drop seems rather uniform, its border is surrounded by a blurry zone where we distinguish some fingering pattern, similar to that observed for an impact on a dry wall (Fig. 6 (a) v) [39]. For impacts on very thin films at low Weber number (We < 1000), the crown does not really fragment, per se, but still breaks into ligaments before retraction actually starts. An example is shown in Fig. 5 (a) i. The spot left by the drop post impact is much blurrier and presents larger, more visible tails due to the coalescence of these ligaments with the film.

B. Crown retraction and decline

Scenario B is observed for high-We impacts on moderately thin films (roughly for $1 \lesssim \delta^\star \lesssim 2$ at We $\gtrsim 2000$) and for thinner films in the case of intermediate We impacts (e.g., for $0.75 \lesssim \delta^\star \lesssim 1.5$ at We $\lesssim 1000$). In the ranges considered the ratio between the viscous and capillary timescales t_ν/t_c approaches 1, while the impact time t_i is very small compared to both t_ν and t_c. The crown formed during the impact is more inclined than in scenario A, but it is not vertical yet (Fig. 6 (b) i) [51]. The diameter of the crown rim is also larger than the diameter of the cavity formed by the crushing drop. As $\delta^\star$ increases and the crown has a longer lifetime, some additional features appear that are shared by scenarios B, C and D. The crown becomes thicker over time and so do the ligaments and ejected droplets [28, 59]. It reaches its maximum height then starts retracting toward its center without tearing apart (Fig 6 (b) ii) as capillary restoring forces overcome inertia. As the transition between the various regimes is not sharp but rather continuous, some incomplete fragmentation might still occur before the end of the retraction phase; otherwise the crown tends to shrink and collapse (Fig 6 (b) iii) [60]. At the very end of this retraction phase only a few thick ligaments reminiscent of the rim collapse in an unpredictable manner, creating random post-impact mixing patterns. While these patterns present a great shape variability, they have a few common features: the spreading distance does not significantly vary and they typically present a more reddish region near the impact point, surrounded by volutes of less concentrated red areas (Figs 5 (b) i and ii, Fig. 6 (b) iv). The red filaments propagating through the crown wall tend to mix more with the fluid coming from the film as they have a longer lifetime (Figs 6 (b) i-ii). Finally, a few capillary ripples can be observed in the film directly surrounding the impact zone (Fig. 6 (b) iii t) [2, 39]. They start from the basis of the crown toward the unperturbed free surface of the film and become wider and last longer as the film gets thicker (Fig. 6 (b) ii-iii). This feature is also exhibited in the following scenarios (Fig. 6 (c) ii-iii and (d) ii-iii). After the crown retraction, these capillary waves dissipate rapidly the remaining kinetic energy from the impact.

C. Jetting

For even thicker films ($\delta^\star \gtrsim 1.5$), the ratio $t_\nu/t_\mathrm{c} \gg 1$, indicating that capillary forces become significant players before the viscous diffusion layer reaches the free surface of the film. The three timescales are ordered as $t_\mathrm{i} < t_\mathrm{c} < t_\nu$. Although the crown behaviour and ensuing mixing pattern depend strongly on the film thickness, for larger $\delta^\star$ the influence of We becomes critical too. At low We ($1 \ll$ We $\lesssim 1000$), because the crown has little kinetic energy, it reaches a relatively small height with an almost vertical inclination (Fig 6 (c) i). It is also much thicker and produces larger and slower secondary droplets (Fig 6 (c) ii) [28, 59]. The peculiarity of these impacts is the uprising central Worthington jet [53, 61] produced at the very end of the retraction phase (Fig 6 (c) iii), similarly to what is observed for deep liquid reservoirs ($\delta^\star > 4$ [35, 56, 57]). It is due to the capillary restoring forces which induce a strong recoil of the crown, pushing all the liquid at once in the center of the cavity.

Ersoy and Eslamian [39] already identified several mechanisms of mixing at play in a range close to ours, as indicated by the white frame in the central diagram of Fig. 5. They covered impacts for We $\in [120\ ;300]$ and $\delta^\star \in [3.5\ ;13.8]$, i.e., with smaller kinetic energies and for thicker films. Nevertheless, similarities exist between such impacts and our measurements in the particular range relative to this section. They observed that expansion-retraction strokes induce mixing directly in the central cavity during the impact, while surface capillary waves propagating outside of this cavity lead to mixing around the impinged area. Ersoy and Eslamian [39] further noted that the motion of the crown wall itself, along with the ejection of secondary droplets, causes an outward flow over the film free surface outside of the crown, further enhancing the mixing. Additionally, we notice in the side view some capillary waves in the crown, just below the rim. They converge back at the impact point where they propagate through the Worthington jet [53], which may enhance its destabilization and pinch off into one or several droplets. The observed mixing patterns present similarities with scenario B: owing to this central jet breaking into droplets that fall back in the film, the central concentrated red area is typically surrounded by more diluted twirls (Figs 5 (c)).

As the transitions between the various observed regimes are not sharp, for thinner films onsets of jets more reminiscent of a mere wave might be visible. Nevertheless, only the waves sufficiently high to produce at least one droplet were considered as actual jets. Calculations performed by Yarin and Weiss [61] predicted no jet emergence between $\delta^\star = 0.04$ and 1, which was later corroborated by Fedorchenko and Wang [35] and corresponds to our observations as well. Premises of jets only appear above $\delta^\star \simeq 1$, and the jet length increases drastically with $\delta^\star$.

D. Crown folding

Again in the thick film region ($\delta^\star \gtrsim 2$), very strong impacts (We $\gtrsim 1000$) lead to the formation of higher crowns also oriented almost vertically (Fig 6 (d) i) [27, 59]. In this case the characteristic timescales are still arranged as $t_\mathrm{i} < t_\mathrm{c} < t_\nu$, although the impact time is much smaller than the capillary time: $t_\mathrm{c}/t_\mathrm{i} \gtrsim 20$ in contrast to $t_\mathrm{c}/t_\mathrm{i} \lesssim 10$ in the former regime. In all the other regimes the crown curvature is mostly oriented outward, but in this case the crown starts bending inward at the end of the growth phase due to capillary forces (Fig 6 (d) ii) [61]. The diameter of the top rim is thus smaller than that of the cavity formed in the film: $r_\mathrm{t}/r_\mathrm{c} < 1$. While in the other cases the retraction starts at the bottom of the crown and propagates to the top, here the crown summit folds and collapses before the crown basis starts retracting. Additional capillary waves may also be observed directly in the crown, right beneath the collapsing rim (Fig. 6 (d) v). In some cases air entrapment at this stage may even cause the appearance of a large bubble [1] having a lifetime of a few seconds (Appendix B 4). While the rim is already collapsing, the basis of the crown still grows and feeds the rim, which consequently thickens excessively and produces massive blobs whose size is comparable with the impacting drop (Fig 6 (d) iii). The interaction between these large portions of fluid seems unpredictable and produces wider mixing patterns, where the red dye seems globally more uniformly concentrated. Although the patterns obtained look irregular, they all consist of a very few twirls whose red borders fade away more gradually in the initial green film than in the other regimes (Figs 5 (d) and 6 (d) iv). Red filaments in the crown are more scarcely distributed than in the former scenarios. The fingering pattern in the cavity formed by the crushed drop is still visible but this time it crosses the interface between the crown and the film (Fig. 6 (d) vi). Some red volutes evenly spread out around the collapsing crown may be observed in the film. Once the collapse comes to an end the convective motion set in the film slightly pushes and mixes up these volutes of red fluid. As depicted in the central diagram of Fig. 5, the transition between scenarios B and C (low We) occurs for smaller $\delta^\star$ than between B and D (high We).

E. Second-order phenomena

Drop impact on thin film at high Weber number displays drop impact-related phenomena generally observed in other contexts, including the aforementioned crown formation and fragmentation, Rayleigh-Taylor and Rayleigh-Plateau instabilities causing the rim break-up into ligaments and subsequent ejected droplets, bubble entrapment or jetting at the end of the retraction phase [1, 2, 57, 61]. A very similar phenomenon to the fingering characteristic of drop impacts on dry wall may also be observed in Figs 6 (a) v and (d) vi [58]. Some additional mixing might be induced away from the central red spot left by the impacting drop due to the ejected droplets which fall back into the film. These droplets may be seen bouncing and coalescing partially or completely before reentering the film [62, 63]. Depending on their concentration, number and distance of ejection, they might induce some additional calcium ion deposition and subsequent growth away from the impact point on actual stalagmites. In the present videos, except for the droplets which fell back very close to the impact point, all these droplets were viewed as an average ejected volume without further consideration.

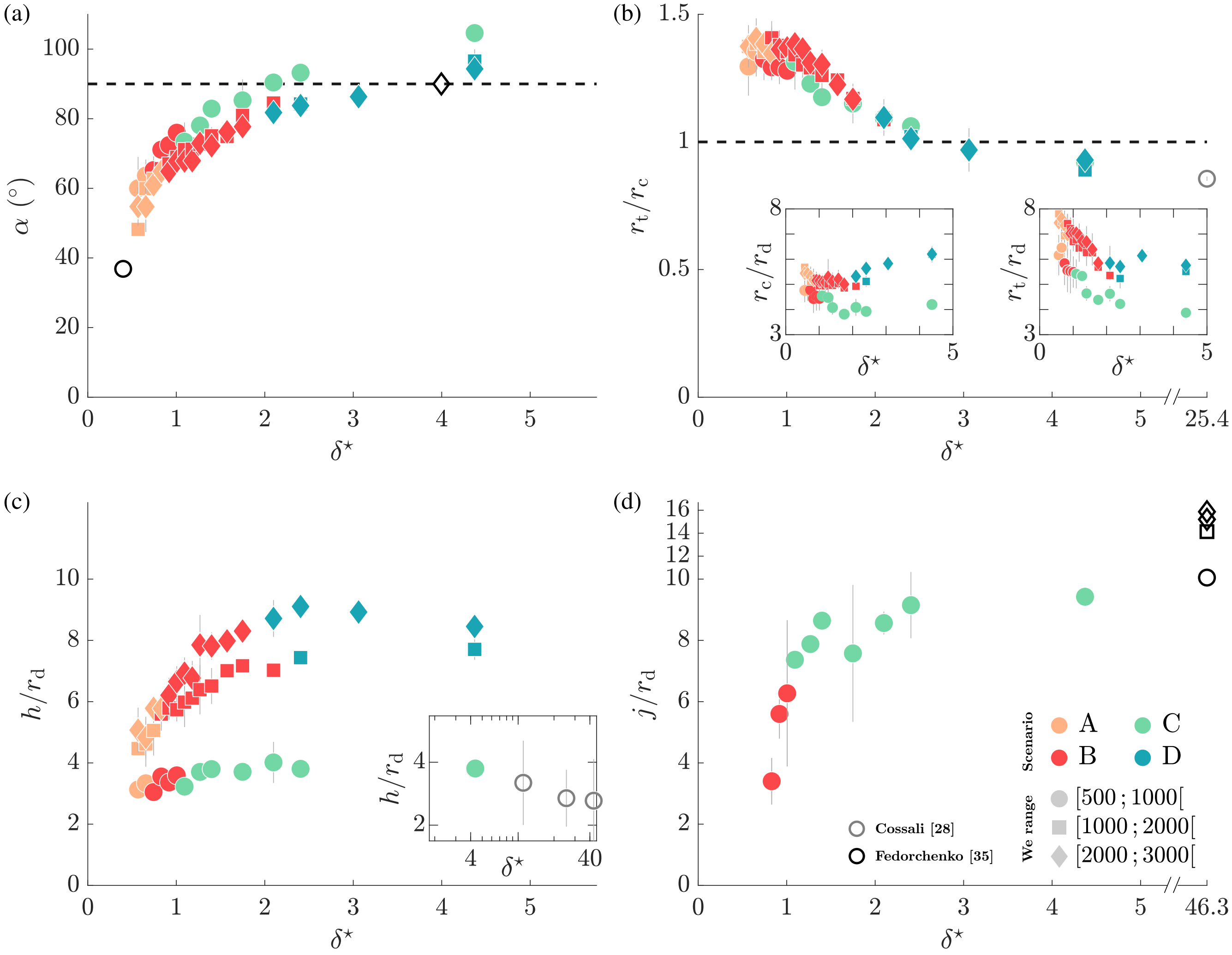

FIG. 7. Crown geometry parameters, as described in Sec. II and in Fig. 1 (b). (a) Average inclination α of the crown during the growth phase (solid symbols). The dotted line corresponds to $\alpha = 90°$. A comparison is made with data from Fedorchenko and Wang [35] for $\delta^\star = 0.4$ and $\delta^\star = 4$ (hollow symbols). (b) Ratio between the radii of the top rim and the cavity expanding in the film, $r_\mathrm{t}/r_\mathrm{c}$ (solid symbols). The hollow symbol shows the value obtained by Cossali et al. [28] for $\delta^\star = 25.4$ with $r_\mathrm{t} = 5.3r_\mathrm{d}$ and $r_\mathrm{c} = 6.2r_\mathrm{d}$. The dotted line shows the case where $r_\mathrm{t} = r_\mathrm{c}$. The insets respectively represent r_t and r_c normalized by the drop radius r_d. (c) Maximum height h reached by the top rim of the crown at various We, normalized by the drop radius r_d (solid symbols). The inset shows the measurement relative to $\delta^\star = 4.4$ from Scenario C, compared to data from Cossali et al. [28] (hollow symbols)), obtained for $\delta^\star \in \{11.1, 25.4, 43\}$. (d) Maximum length j of the jet emitted following the crown retraction at low We, normalized by the drop radius r_d. A comparison is made with data from Fedorchenko and Wang [35] for $\delta^\star = 46.3$ at various We. All measurements are shown as a function of the non-dimensional film thickness $\delta^\star$. The legend from (d) is the same for all four graphs. Symbols correspond to various intervals of We: circles for We < 1000, squares for $1000 <$ We < 2000, and diamonds for We > 2000. The color of the symbols refers to the scenarios described in Section III.

IV. MEASUREMENTS

This section presents the measurements obtained from the side and top views of the impacts, as described in Sec. II. The first part focuses on the crown geometry observed from side-view high-speed movies. The second part of the section aims at describing the mixing between the drop and the film using the top view of the impacts. All subsequent graphs are represented as a function of the non-dimensional film thickness $\delta^\star$ and for various bins of We. One symbol in the graph shows the mean ± s.d. over an ensemble of 4 to 5 points, on average, obtained for close $\delta^\star$ and We values and considered as belonging to the same bin. Some points in the graph exhibit a very small standard deviation or may not have one in the uncommon cases (5 % of all the measurements) where there is only one measurement in the corresponding ($\delta^\star$, We) bin. The range of δ is divided in 10 μm

($\Delta\delta^\star = 0.086$) wide bins between 60 µm ($\delta^\star = 0.5$) and 170 µm ($\delta^\star = 1.5$). Then the width of the bins is progressively increased up to $\delta = 500\,\mu$m ($\delta^\star = 4.3$). In terms of Weber number, the smallest bin, for We $\in]500\,;\,1000]$, corresponds to the impacts after which jetting is observed for thicker films, i.e., when $\delta^\star \gtrsim 1.5$ (Fig. 6 (c)) while the highest one, for We $\in [2000\,;\,3000[$, shows the impacts for which the crown folds upon itself before retracting when $\delta^\star \gtrsim 2$ (Fig. 6 (d)). The third bin represents the intermediate values, namely the transitional regime (Fig. 6 (b)). For very thin films ($\delta^\star < 1$), no matter the Weber number the scenario is always the same and corresponds to the crown fragmentation (Fig. 6 (a)).

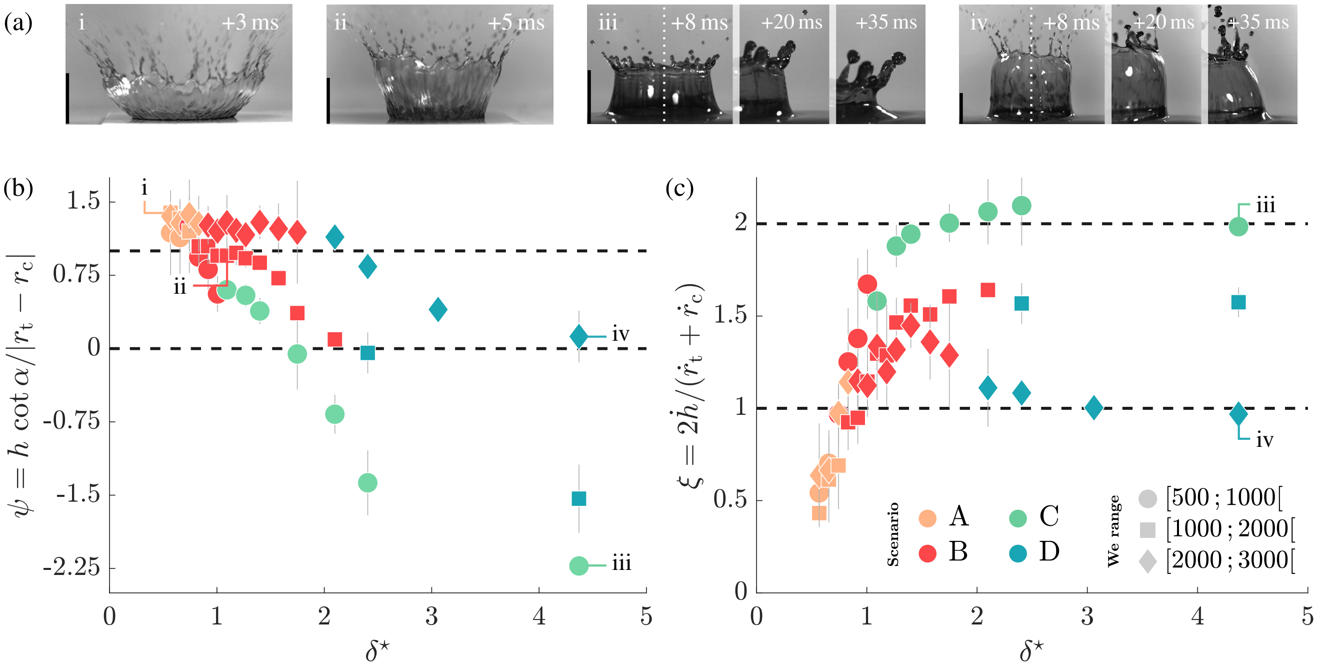

FIG. 8. Crown shape factor and retraction velocity components. (a) Examples of crown shapes shown in the graph of (b): i. $\delta^\star = 0.56$, We $= 1675$, shape factor of 1.39, ii. $\delta^\star = 1.1$, We $= 1675$, shape factor of 1.09, iii. $\delta^\star = 4.3$, We $= 525$, shape factor of -2.24 and average velocity ratio of 1.98, and iv. $\delta^\star = 4.3$, We $= 2740$, shape factor of 0.37 and average velocity ratio of 0.95. Two frames showing the main retraction direction of the crown are added in iii and iv, with a correspondence in the graph from (c). The scale bars are 1 cm. (b) Crown shape factor ψ, and (c) ratio of crown retraction velocity components ξ, both computed as a function of the non-dimensional film thickness $\delta^\star$. The dashed line from (b) at $\psi = 0$ corresponds to a change of sign when $\alpha = 90°$. The other dashed line at $\psi = 1$ corresponds to the change from a crown convex profile to a straight profile. In (c) the two dashed lines are drawn at $\xi = 1$ and $\xi = 2$. The symbol colors correspond to the scenarios identified in Section III. The legend is the same in both graphs.

A. Crown geometry

Measurements obtained from the side view of the impacts are described in Fig. 1 (b) and reported in Fig. 7. Figure 7 (a) shows the average inclination angle α of the crown during the growth phase, i.e., between 2 ms and 10 ms after the beginning of the impact (or 6 ms in Scenario A). This inclination increases with $\delta^\star$ and exceeds 90° for $\delta^\star \gtrsim 2$. In Fig. 7 (b) we report the ratio between the maximum radial extension of the top and bottom of the crown, $r_\mathrm{t}/r_\mathrm{c}$ (the maximum being computed as the average of the 5 largest measurements). It decreases with increasing δ^* and becomes lower than 1 for $\delta^* \gtrsim 2$, in accordance with the evolution of α. Figure 7 (c) represents the maximum height h reached by the crown. Since for small film thickness ($\delta^\star \lesssim 2$), the ratio $r_\mathrm{t}/r_\mathrm{c}$ is more or less constant while α increases, the maximum height h reached by the crown increases as well. The maximum height h then seems to reach a limit value at large film thickness ($\delta^\star \gtrsim 2$). While α and $r_\mathrm{t}/r_\mathrm{c}$ are almost independent of We, the maximum height reached by the crown is greatly affected by We as it goes from $3.6\,r_\mathrm{d}$ to $10.3\,r_\mathrm{d}$ when $\delta^\star \gtrsim 2$ (averages obtained with respectively the 5 largest and smallest measurements). Figure 7 (d) shows the evolution of the maximum length j of the jet protruding from the film in scenario C, before it pinches off. Although the maximum height reached by the crown in scenario C is small, the maximum length of the jet compares to the height of the crown from scenario D. Very short jets are already observed for some experiments when $\delta^\star \lesssim 1.5$, but not systematically. Their length seems to increase sharply with $\delta^\star$ when $\delta^\star \simeq 1$, then slowly once $\delta^\star \gtrsim 1.5$. The graphs from Fig. 7 are completed using data obtained by Fedorchenko and Wang [35] (α, j), and by Cossali et al. [28] ($r_\mathrm{t}/r_\mathrm{c}$, h) in a similar range to ours. Except for one value of α taken at $\delta^\star = 0.4$, these data usually correspond to the upper limit of our range, with $\delta^\star \gtrsim 4$. They are in good agreement with our observations. The jet was also reported and measured by Fedorchenko and Wang [35] for a very large film thickness ($\delta^\star = 46.3$) at $\mathrm{We} > 1000$, which is typically observed in the deep pool limit of impacts on wetted walls [29, 53, 54].

From these geometrical measurements we may define a crown shape factor as $\psi = h\cot\alpha / |r_\mathrm{t} - r_\mathrm{c}|$. The evolution of this quantity is shown in Fig. 8 (b). For $\delta^\star < 1$, the crown shape is more or less the same for all We. But then as the film thickness increases beyond $\delta^\star = 1.5$, the shape factor decreases with increasing $\delta^\star$, and it does more sharply for lower We. When the ratio ψ is close to 1, the crown profile almost looks like a straight line (Fig. 8 ii). When the shape factor is larger than 1, the inclination α made by the crown interface is smaller than $\operatorname{arccot}(|r_\mathrm{t} - r_\mathrm{c}|/h)$, i.e., the corresponding crown has a convex profile. By contrast, a value of ψ smaller than 1 represents the opposite case, i.e., a concave crown shape. These two cases are illustrated in Fig. 8 (a) i and iii, respectively. The change of sign in ψ corresponds to the case where $\alpha > 90°$ (Figs 8 iii and iv). In the thin film region ($\delta \lesssim 1$), the crown thus typically takes a convex shape, while in the thick film region ($\delta \lesssim 2$) there is a change of curvature or even a crown whose bottom spreads out more than the top rim.

One might also compare the vertical (from top to bottom) and radial (inward) retraction velocities of the crown. The vertical retraction velocity $\dot{h}$ is estimated right after the maximum height is reached in each experiment. The radial component corresponds to the average of $\dot{r}_\mathrm{t}$ and $\dot{r}_\mathrm{c}$, again measured right after both radii reach their maximum. Estimations of the ratio $\xi = 2\dot{h}/(\dot{r}_\mathrm{t} + \dot{r}_\mathrm{c})$ are taken for each experiment by using the derivatives of quadratic fits made on the $h(t)$, $r_\mathrm{t}(t)$ and $r_\mathrm{c}(t)$ curves, obtained between t_c and $t_\mathrm{c} + 5\,\mathrm{ms}$. On average for all the experiments in a given scenario, the maximum in the $h(t)$, $r_\mathrm{t}(t)$ and $r_\mathrm{c}(t)$ curves is observed at about the same time. This time has a value of $16.4 \pm 2.7\,\mathrm{ms}$ on average for all the impacts in the central jet case (scenario C, $\mathrm{We} \lesssim 1500$) and $14 \pm 1.4\,\mathrm{ms}$ in the crown folding case (scenario D, $\mathrm{We} \gtrsim 1500$), so both are very close to t_c. The ratio ξ is equal to 2.06 ± 0.21 in the jetting case and to 1.13 ± 0.28 in the crown folding case (averages ± s.d. of all the experiments corresponding to scenarios C and D, respectively). In other words, in scenario C the crown height decrease occurs much faster than the radial retraction, which then continues in the film after the crown has disappeared and allows for the jet to protrude. On the contrary, in scenario D both components of the retraction velocity are similar, hence the folding observed. These measurements correspond to the observations from Figs 6 (c-d) i and ii. The evolution of the ratio ξ with the film thickness is shown in Fig. 8 (c). At low and intermediate We, this ratio increases with the film thickness for $\delta^\star \lesssim 1.5$. Then for $\delta^\star \gtrsim 1.5$ it reaches a limit value which is larger at lower We. For the highest We, a maximum is observed around $\delta^\star \simeq 1.5$ then a limit value close to 1 is reached in the thick film region. Two short sequences from scenarios C and D are shown in Figs 8 (a) iii and iv, respectively, where the difference in the retraction motion of the two crowns is visible.

B. Mixing and thickness variations

Mixing level indicators may be inferred from the film thickness variation and red proportion maps taken after each impact (Figs 2 (b) and (c)). We first consider the physical extension and scattering of the spot left by the drop in the film post-impact. We then deduce the quantity of water ejected during the impact, as well as the average proportion coming from the initial drop into the ejections.

1. *Equivalent moments of the red dye proportion distribution*

The red spot left in the film by the crushed drop varies greatly in shape and size (see Fig. 5). To estimate the size variations of this spot, we first define the k^th-order moment of the red dye proportion in the film as follows:

$$M_k = \int_0^{2\pi} \int_0^{\infty} p_r(r,\theta)\, r^{k+1}\, \mathrm{d}r\, \mathrm{d}\theta\,, \tag{1}$$

where r and θ denote the cylindrical coordinates in a frame centered at the impact point (Fig. 9 (b) i). The impact point position is measured in the high-speed color videos, at the closest frame right after the drop starts crushing. The red dye concentration p_r is measured at about 1 s after the impact, as shown in the example of Fig. 2 (b). The normalized first-order moment represents an equivalent red spot radius R_eq, defined as

$$R_\mathrm{eq} = \frac{M_1}{M_0}\,. \tag{2}$$

Using the normalized second-order moment, it is likewise possible to define the variance of the distribution as

$$\sigma_\mathrm{eq}^2 = \frac{M_2}{M_0} - R_\mathrm{eq}^2\,. \tag{3}$$

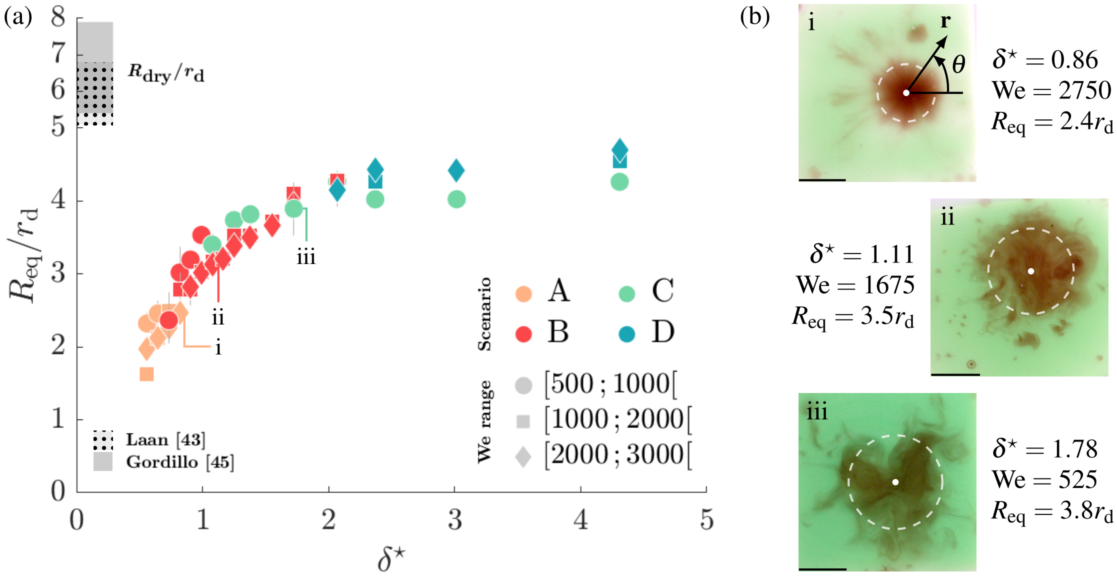

FIG. 9. Non-dimensional equivalent radius R_{eq} of the red stain left by the drop in the film, defined in Eq. (2): (a) Measurements of R_{eq} as a function of the non-dimensional initial film thickness $\delta^\star$, divided in three bins of We. The gray and dotted bands represent the maximum spatial extension $R_{\mathrm{dry}}/r_{\mathrm{d}}$ reached by a drop on a dry wall between We $= 500$ and We $= 3000$. These boundaries are estimated using the results from Laan et al. [43] (dots) and Gordillo et al. [45] (plain), respectively. The symbol colors correspond to the scenarios observed in Section III. The roman lowercase letters show the location of the examples from (b) in the graph. (b) Examples of radii computed according to Eq. (2) and superimposed with the corresponding initial photographs, for the following ranges of parameters: i) very thin film, high We, ii) thin film, intermediate We and iii) thick film, low We. Picture i also shows the (r, θ) coordinates used to compute the integral from Eq. (2). The equivalent radius and drop impacting point are represented in each photograph by a white dashed circle and a white dot, respectively. The scale bars are 1 cm.

If the red proportion distribution is a Dirac function centered in $r = R^\star$, then $R_{\mathrm{eq}} = R^\star$ and $\sigma_{\mathrm{eq}} = 0$. If the distribution is uniform for $r \leq R^\star$ and null for $r > R^\star$, then $R_{\mathrm{eq}} = 2/3 R^\star$ and $\sigma_{\mathrm{eq}} = R^\star/(3\sqrt{2})$. The evolution of the equivalent red spot radius R_{eq} with $\delta^\star$ is shown in Fig. 9 (a), for the same three bins of We as in the previous section. Figure 9 (b) shows examples of the radii obtained in several cases, which are drawn directly in the corresponding pictures. For the sake of comparison, the maximum radius that would be reached by a drop colliding with a dry wall, R_{dry}, is also represented in Fig. 9 (a). The dry radius R_{dry} increases with We, hence it is represented as a band corresponding to the bin We $\in [500; 3000]$ with estimations from Laan et al. [43] and Gordillo et al. [45], respectively. In the same manner, Fig. 10 (a) shows the evolution of σ_{eq} with $\delta^\star$, with illustrations in Fig. 10 (b).

We observe in Fig. 9 (a) that R_{eq} increases monotonously with the initial film thickness $\delta^\star$ and reaches a limit value at $\delta^\star \gtrsim 2$. The radii measured at $\delta^\star < 1$ are small compared to the dry radius R_{dry}. Additionally, the variation of the radius with We is less pronounced when there is a film than when there is none [42, 58]. The dry radius R_{dry} indeed goes from $5.3 r_{\mathrm{d}}$ at We $= 500$ to $7.5 r_{\mathrm{d}}$ at We $= 3000$ (averages obtained with [43, 45]). On the other hand, the largest difference observed between R_{eq} values at a given thickness range for We $= 500$ and We $= 3000$ is of about $0.4 r_{\mathrm{d}}$. We get rid of the $\delta^\star$ dependence by defining $R_{\mathrm{eq}}(\mathrm{We}) = R_{\mathrm{eq}}(\delta^\star, \mathrm{We})/\overline{R_{\mathrm{eq}}}(\delta^\star)$, i.e., each radius measurement corresponding to one experiment is normalized by the average made on all the measurements corresponding to its bin of $\delta^\star$, disregarding We. An anova test performed for $R_{\mathrm{eq}}(\mathrm{We})$ (i.e., for all We from Section III rather than for the three bins of Fig. 9) yields a p-value of 2×10^{-5}. The influence of We on R_{eq} is thus statistically significant although it is lesser than the influence of $\delta^\star$. The correlation coefficient between the normalized $R_{\mathrm{eq}}(\mathrm{We})$ and all the We from Section III is -0.33, i.e., the equivalent radius slightly decreases when We increases. This is visible in Fig. 9 (a) up to $\delta^\star \lesssim 2$, the corresponding bins representing most experiments (14 bins out of 17 bins of $\delta^\star$). The standard deviation σ_{eq} also increases with $\delta^\star$, as seen in Fig. 10 (a). In the same manner as R_{eq}, the value of σ_{eq} is very small for $\delta^\star \lesssim 1$, while it reaches a more or less stationary value when $\delta^\star \gtrsim 2$. An anova test performed on $\sigma_{\mathrm{eq}}(\mathrm{We})$ in the same manner as for $R_{\mathrm{eq}}(\mathrm{We})$ gives a p-value of 8×10^{-3}, i.e., the influence of We on σ_{eq} seems significant. The correlation coefficient of $\sigma_{\mathrm{eq}}(\mathrm{We})$ is -0.20, so σ_{eq} also decreases slightly with We. The inset of Fig. 10 shows the second-order moment σ_{eq} over the equivalent radius R_{eq}. They were computed for each experiment, then divided into bins and averaged. By averaging the measurements corresponding to the four scenarios identified in the previous section, we obtain the following values for $\sigma_{\mathrm{eq}}/R_{\mathrm{eq}}$: A) $37.6 \pm 2.7\,\%$, B) $44.1 \pm 1.8\,\%$, C) $43.7 \pm 0.8\,\%$, and D) $45.6 \pm 2.1\,\%$ (average ± s.d. on all measurements corresponding to a

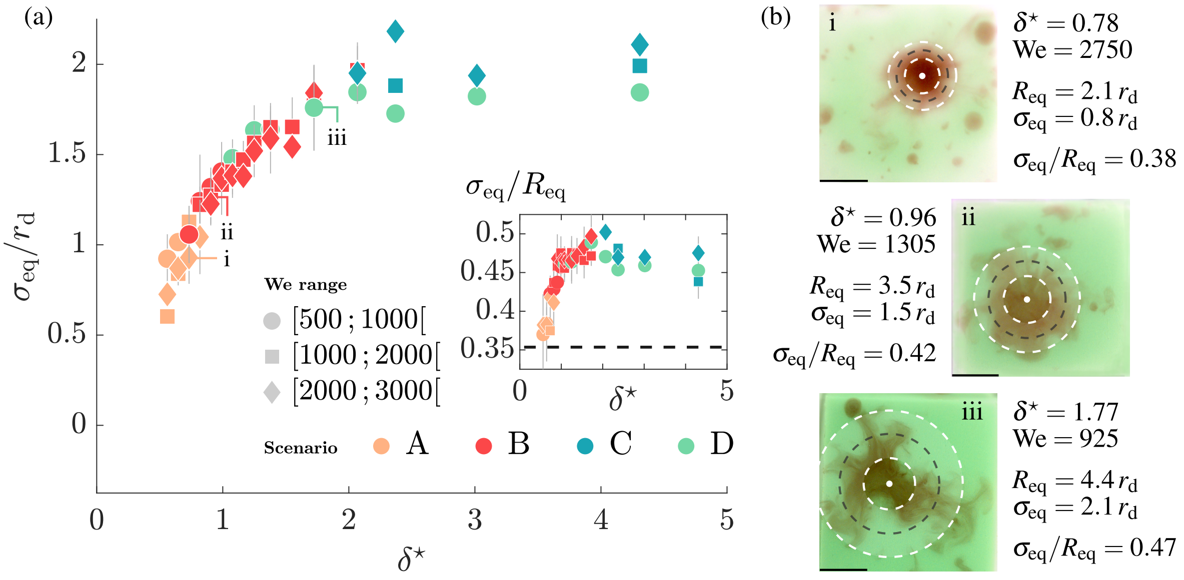

FIG. 10. Non-dimensional second order moment σ_{eq} of the red proportion in the film post impact, defined in Eq. (3): (a) Measurements of σ_{eq} as a function of the non-dimensional initial film thickness $\delta^\star$, for three bins of We. The colors represent the various scenarios described in Section III. The roman lowercase letters show the locations of the examples from (b) in the graph. The inset represents the second-order moment divided by the equivalent radius, $\sigma_{\mathrm{eq}}/R_{\mathrm{eq}}$. The dashed line in the inset corresponds to the theoretical uniform distribution value of $1/(2\sqrt{2})$. (b) Examples of radii R_{eq} (dashed, black) and $R_{\mathrm{eq}} \pm \sigma_{\mathrm{eq}}$ (dashed, white) superimposed with the corresponding initial photographs, for the following ranges of parameters: i) very thin film, high We, ii) thin film, intermediate We and iii) thick film, low We. The white dots show the impact points. The scale bars are 1 cm.

given scenario, see Fig. 5). The variation of the area covered by the red stain in the film is thus less pronounced in scenario A than in the others, and is also closer to the theoretical uniform distribution case for which $\sigma_{\mathrm{eq}}/R_{\mathrm{eq}} = 1/(2\sqrt{2}) \simeq 35\,\%$. In scenarios B, C and D, the order of magnitude of $\sigma_{\mathrm{eq}}/R_{\mathrm{eq}}$ is the same, although a small difference may be observed between scenarios C and D.

2. *Ejected volume*

We infer both the total ejected volume during the impact and the drop proportion left in the film from the raw measurements of film thickness and red dye proportion (see Fig. 2). As described in Fig. 11, we denote the impacting drop volume V_{d}, the initial film volume V_{f} and the final film volume $V_{\mathrm{f'}}$. This film has a supposedly uniform thickness δ before the impact and unknown thickness δ' after the impact, where the latter may vary in space. The total volume of all the ejected droplets is V_{e}. The drop volume V_{d} may be split into two contributions: one going into the impacted film, $V_{\mathrm{d}\to\mathrm{f'}}$, an the other going into the ejections, $V_{\mathrm{d}\to\mathrm{e}}$. The same holds for the initial film volume V_{f} that we may split into the part $V_{\mathrm{f}\to\mathrm{f'}}$ remaining in the film and the part $V_{\mathrm{f}\to\mathrm{e}}$ that joins the ejected droplets. The total ejected volume V_{e} therefore corresponds to $V_{\mathrm{d}\to\mathrm{e}} + V_{\mathrm{f}\to\mathrm{e}}$, whereas the film volume after impact $V_{\mathrm{f'}}$ is equal to $V_{\mathrm{f}\to\mathrm{f'}} + V_{\mathrm{d}\to\mathrm{f'}}$. We call φ_{e} the ejected ratio, namely the ratio of the total ejected volume V_{e} over the impacting drop volume V_{d}, and write

$$\varphi_{\mathrm{e}} = \frac{V_{\mathrm{d}\to\mathrm{e}} + V_{\mathrm{f}\to\mathrm{e}}}{V_{\mathrm{d}}} = 1 - \frac{(V_{\mathrm{d}\to\mathrm{f'}} + V_{\mathrm{f}\to\mathrm{f'}}) - (V_{\mathrm{f}\to\mathrm{e}} + V_{\mathrm{f}\to\mathrm{f'}})}{V_{\mathrm{d}}} = 1 - \frac{V_{\mathrm{f'}} - V_{\mathrm{f}}}{V_{\mathrm{d}}} = 1 - \frac{1}{V_{\mathrm{d}}} \int_S \left(\delta' - \delta\right) \mathrm{d}S\,. \tag{4}$$

The integration domain S corresponds to the 40×40 cells on which δ and p_r are obtained by colorimetry (see Fig. 2 (c)). In practice it is equivalent to a 35-40 mm side square, which is sufficiently large to take into account the thickness variations and yield an almost null difference $(\delta' - \delta)$ away from the impacted area (see Fig. 2 (c)). By averaging $|\delta' - \delta|$ over all the cells outside a disk of radius $2R_{\mathrm{eq}}$ centered on the impact point, we obtain values going from $0.05\,\mu$m to $5\,\mu$m (averages of 30 best and worst cases), with a mean for all the experiments of $3\,\mu$m. Most of the worst cases correspond to the thinner films ($\delta^\star \lesssim 1$), for which the lighting may induce some errors on the edges of the pictures (see Section II B). The integration domain is also sufficiently small so that the ejected droplets that could fall into the film are neither seen in the pictures nor taken into account [28]. The only exceptions are the very slow and large droplets which induce mixing directly in the impacted zone at the

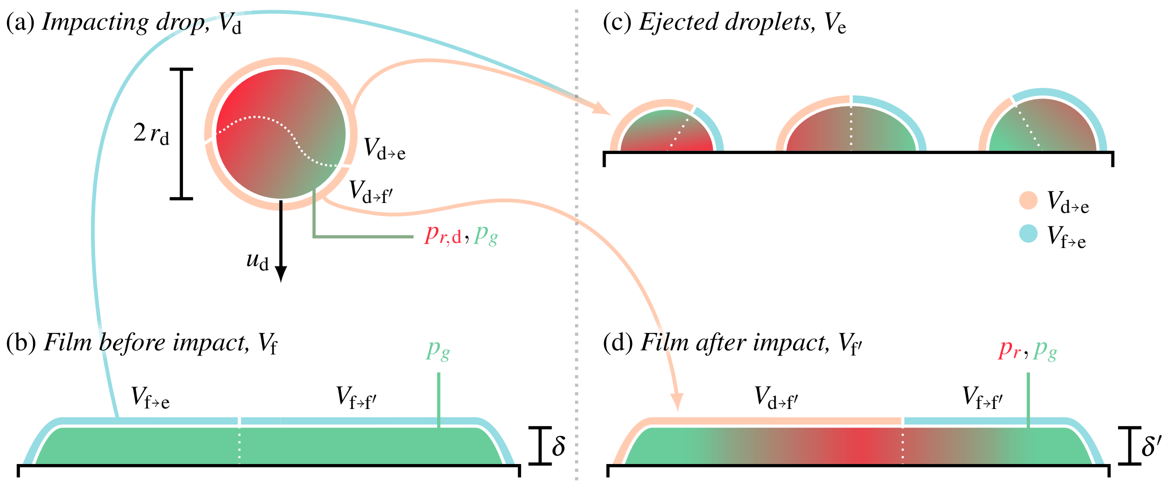

FIG. 11. Drop, film, dye proportions and volume distribution nomenclature. (a) Impacting drop containing both red and green dyes in respective proportions $p_{r,\mathrm{d}}$ and p_g. The drop has a radius r_d, a final velocity u_d and a volume V_d split into two contributions: $V_{\mathrm{d}\to\mathrm{e}}$ which goes into the ejections, and $V_{\mathrm{d}\to\mathrm{f}'}$ which remains in the film after the impact. (b) Initial film containing only green dye in proportion p_g, of supposedly uniform thickness δ and of volume V_f divided into $V_{\mathrm{f}\to\mathrm{e}}$, the ejected part, and $V_{\mathrm{f}\to\mathrm{f}'}$, the remaining part. (c) Post-impact ejected droplets of unknown red volume fraction and of total added volume V_e coming from the sum of $V_{\mathrm{d}\to\mathrm{e}}$, the ejected volume initially in the drop, and $V_{\mathrm{f}\to\mathrm{e}}$, the ejected volume initially contained in the film. (d) Post-impact film of both unknown thickness δ' and red proportion p_r, and of known green proportion p_g. Its volume $V_{\mathrm{f}'}$ corresponds to the addition of $V_{\mathrm{d}\to\mathrm{f}'}$, the volume going from the impacting drop into the film, and $V_{\mathrm{f}\to\mathrm{f}'}$, the part already in the film before the impact and which has not been ejected.

end of the crown retraction or jet pinch-off. For very large film thicknesses ($\delta^\star \gtrsim 4$), as shown by, e.g., Figs 5 (d) and 10 (b) iii, the surroundings of the impacted area might sometimes be truncated when this area has a size close to S, although cases with a very visible truncation were left apart (see Appendix B 4). Around $\delta^\star \simeq 4$, the colorimetry hypotheses become less valid (see Appendix B 3 b) and there are fewer experiments. Although the exact results relative to these cases should thus be taken with precaution, they should not affect the conclusions relative to the following graphs.

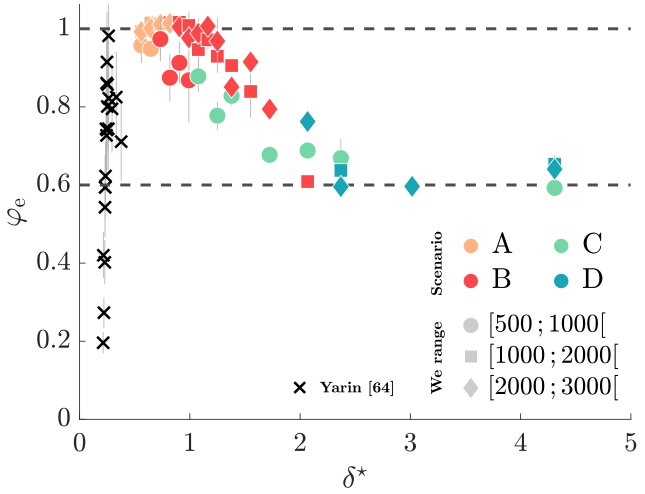

FIG. 12. Ejected ratio φ_e from Eq. (4), corresponding to the total ejected volume V_e over the impacting drop volume V_d, as a function of $\delta^\star$ and for various bins of We. The dashed lines represent limit values exhibited by this ratio, i.e., $\varphi_\mathrm{e} = 0.6$ and $\varphi_\mathrm{e} = 1$. The colors correspond to the different scenarios observed and described in Section III. The black crosses represent data from Yarin and Weiss [64], adapted to our experimental range by using $\mathrm{Oh} = 1.7 \times 10^{-3}$ and $\mathrm{We} = 1500$.

Figure 12 shows the ejected proportion φ_e as a function of $\delta^\star$. Our values are shown for $\delta^\star \geq 0.56$ (solid symbols) and compared to data from Yarin and Weiss [64] taken above the splashing threshold. These authors computed φ_e by summing the volume of all the secondary droplets that they measured in their experimental photographs, V_e, and by dividing this sum by the impacting drop volume V_d. They did not represent their experimental values as a simple function of the Weber number or non-dimensional film thickness, but rather as a function of the combination $u = \mathrm{We}^{1/2}\,(\delta^\star)^{3/4}\,\mathrm{Oh}^{-1/8}$. Their range of parameters is such that $\mathrm{Oh}_\mathrm{Yarin} = 1.8\times10^{-2}$, $\mathrm{We}_\mathrm{Yarin} \in [250;1500]$ and $\delta^\star_\mathrm{Yarin} \in [0.8;2]$, with the ejected proportion measured between $u = 18.4$ and $u = 32.4$. To adapt this to our range of parameters, we used $\mathrm{Oh} = 1.7\times10^{-3}$ and $\mathrm{We} = 1500$, and inferred from u that $\delta^\star \in [0.21;0.38]$. We also represented their error bars which were estimated at 14 % of φ_e. As seen in Fig. 12, the ejected proportion first increases sharply with $\delta^\star$, going from an almost null value to about 1. Then, for $\delta^\star \gtrsim 1$, the proportion φ_e decreases with increasing $\delta^\star$ and reaches a limit value of about 0.6 at large film thickness, i.e., such that $\delta^\star \gtrsim 2$. This behaviour seems approximately independent of We. In other words, the film volume post-impact $V_{\mathrm{f}'}$ is larger ($\varphi_\mathrm{e} < 1$) than the initial volume V_f, though only slightly ($\varphi_\mathrm{e} \simeq 1$) around $\delta^\star \simeq 1$. In this case, as much liquid is ejected as brought by the incoming drop. The average film thickness therefore remains constant although it is no longer uniform in space 1 s after the impact (see Fig. 2 (c)). At lower film thickness in our data (solid symbols), it is difficult to distinguish the results obtained for the two highest bins of We ($\mathrm{We} > 1000$), but the measurements corresponding to scenario C overall seem to exhibit a lower ejected proportion (i.e., a larger volume going into the film at small We). Additionally, our data are in the continuity of data from Yarin and Weiss [64]. The maximum value reached by φ_e for thin films in our range is 1.03 with a relative error of 2 % (average on 5 largest measurements). The average relative error in our measurements is 5 %.

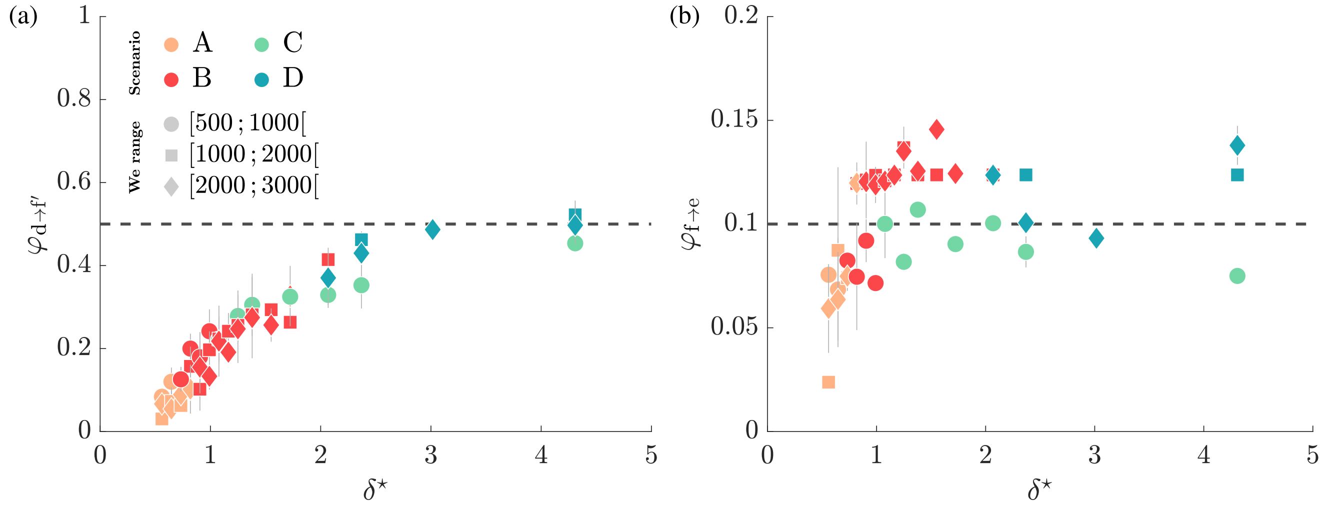

FIG. 13. (a) Proportion of the volume coming from the drop left in the film after the impact, $\varphi_{\mathrm{d}\to\mathrm{f}'}$, as defined in Eq. (5). The dashed line shows the limit case for which $\varphi_{\mathrm{d}\to\mathrm{f}'} = 0.5$. (b) Ratio of the film volume lost in the ejections over the initial drop volume, $\varphi_{\mathrm{f}\to\mathrm{e}}$, as defined in Eq. (6). The dashed line shows the case for which $\varphi_{\mathrm{f}\to\mathrm{e}} = 0.1$. Measurements are shown as a function of the film thickness $\delta^\star$ and for three bins of We. The colors correspond to the different scenarios observed and described in Section III. The legend is the same in both graphs.

3. *Drop proportion left in the film post-impact*

The proportion of the impacting drop that remains in the film after impact is defined as the ratio of the volume coming from the drop and remaining in the film following the impact, $V_{\mathrm{d}\to\mathrm{f}'}$, over the impacting drop volume V_d:

$$\varphi_{\mathrm{d}\to\mathrm{f}'} = \frac{V_{\mathrm{d}\to\mathrm{f}'}}{V_\mathrm{d}} = \frac{1}{V_\mathrm{d}}\int_S \frac{p_r\,\delta'}{p_{r,\mathrm{d}}}\,\mathrm{d}S\,. \tag{5}$$

Although the integration domain S is arbitrary, it is much larger than the impinged area. As it may be seen in Fig. 2 (b), the red proportion in the film p_r is zero far from this zone, i.e., when $r > R_\mathrm{eq} + \sigma_\mathrm{eq}$. Contributions to the integral are thus negligible away from the impact region and the choice of S does not affect the computed integral, except in the already discussed case of very thick films for which $\delta^\star \gtrsim 4$. The evolution of $\varphi_{\mathrm{d}\to\mathrm{f}'}$ with $\delta^\star$ is shown in Fig. 13 (a). We observe that $\varphi_{\mathrm{d}\to\mathrm{f}'}$ overall increases with the film thickness. The Weber number does not seem to significantly influence this evolution. At $\delta^\star < 1$, the proportion of the drop left in the film post impact is quite small, about 0.1. Hence, a large amount of the initial drop volume ends up in the ejections. Then $\varphi_{\mathrm{d}\to\mathrm{f}'}$ increases with $\delta^\star$, such that the proportion of the impacting drop going into the ejections decreases. For $\delta^\star \gtrsim 2$, the ratio $\varphi_{\mathrm{d}\to\mathrm{f}'}$ also appears to reach a stationary value of about 0.5.

The sum of the two latter quantities can be related to another proportion:

$$\varphi_{\mathrm{f}\to\mathrm{e}} = \frac{V_{\mathrm{f}\to\mathrm{e}}}{V_\mathrm{d}} = (\varphi_\mathrm{e} + \varphi_{\mathrm{d}\to\mathrm{f}'}) - 1\,. \tag{6}$$

The proportion $\varphi_{\mathrm{f}\to\mathrm{e}}$ compares the volume of fluid initially in the film and ejected away at impact, to the fixed drop volume. It is shown as a function of $\delta^\star$ in Fig. 13 (b). The variations in the graph should mostly come from additive numerical errors, given that this ratio is calculated from other numerical values rather than raw measurements. We observe that $\varphi_{\mathrm{f}\to\mathrm{e}}$ remains close to 0.1. Little fluid originating from the film therefore goes into the ejections. In other words, most of the initial film fluid remains in the film.

V. DISCUSSION

The differences between scenarios observed qualitatively are also visible in the measurements described in the previous section. The main difference between the scenarios is the ordering of the capillary and viscous diffusion timescales t_c and t_ν. In scenario A ($\delta^\star < 1$) the high kinetic energy of the drop is mostly transferred to the top part of the expanding crown. At the same time viscous forces quickly slow down the motion of the crown near the film. Since nothing prevents the further extension of the top part of the crown ($t_\nu < t_\mathrm{c}$), fragmentation occurs due to the large velocity gradients appearing between the top and the bottom of the crown. Then, as the thickness is increased ($\delta^\star \gtrsim 1$), retraction of the crown is observed in scenario B. The expanding crown is again slowed down at its basis due to the viscous forces propagating from the solid surface to the free liquid surface of the film. But at the same time, given that $t_\nu \sim t_\mathrm{c}$, capillary forces tend to shrink the crown. Increasing further the film thickness ($\delta^\star \gtrsim 2$), the crowns obtained in scenarios C and D are oriented perpendicularly to the film free surface, or even start bending inward before completing their expansion phase. The capillary forces act sooner than the viscous forces in the film ($t_\mathrm{c} < t_\nu$), thereby preventing a large extension of the crown top part as in the first two scenarios, while dissipation in the film only slows down the crown basis later.

Following these observations, it is not surprising to see that all the crown geometry parameters and mixing level indicators depend strongly on $\delta^\star$, and that most mixing level indicators are correlated to the crown geometry (see Table I). In scenario A, the viscous dissipation slowing down the crown basis translates into a very inclined and convex-looking crown, which is corroborated by the measurements of α, $r_\mathrm{t}/r_\mathrm{c}$, h and of the crown shape factor $\psi > 1$ (Figs 7 and 8). Regarding the post-impact mixing in scenario A, the red dye is distributed on a very small radius R_eq, in an almost uniform manner given that $\sigma_\mathrm{eq}/R_\mathrm{eq}$ is close to the theoretical uniform distribution in this case. Such a distribution is consistent with the fragmentation of the crown observed and the viscous dissipation occurring rapidly, thereby preventing any further convective motion in the film that would lead to more mixing. In scenario B, measurements relative to the crown geometry correspond to the balance between the viscous dissipation and capillary forces, which yields a shape factor ψ close to 1. Because of the crown retraction at the end of the impact, mixing is increased and larger values are obtained for both R_eq and σ_eq. The ejected volume proportion φ_e is close to 1 in scenario A, i.e., there is as much liquid ejected away during the impact as in the incoming drop. The ejections also mostly contain liquid from the drop as the proportion of drop liquid in the ejections corresponds to $1 - \varphi_{\mathrm{d}\to\mathrm{f}'} \gtrsim 0.9$. Then, as $\delta^\star$ increases and fragmentation is no longer observed (scenario B), φ_e decreases while $\varphi_{\mathrm{d}\to\mathrm{f}'}$ increases, i.e., there is a larger proportion of the drop going into the film and a smaller one into ejections, which also represent a lower total volume.

TABLE I. Correlation coefficients between the mixing level indicators (equivalent moments R_eq and σ_eq, ejected proportion φ_e, proportion of the drop volume going into the film $\varphi_{\mathrm{d}\to\mathrm{f}'}$, and proportion of the film going into the ejections $\varphi_{\mathrm{f}\to\mathrm{e}}$) and the crown geometry parameters (inclination α, ratio of top and bottom radii $r_\mathrm{t}/r_\mathrm{c}$ and height h), compared with the correlation coefficients obtained between the mixing level indicators and $\delta^\star$.

Mixing and thickness variation	**Crown geometry**			**Thickness**
	α	$r_\mathrm{t}/r_\mathrm{c}$	h	$\delta^\star$
R_eq	0.96	-0.86	0.50	0.88
σ_eq	0.93	-0.84	0.56	0.87
φ_e	-0.86	0.95	-0.28	-0.90
$\varphi_{\mathrm{d}\to\mathrm{f}'}$	0.91	-0.88	0.44	0.90
p	0.42	-0.18	0.63	0.36

In scenario C and D, because the capillary forces act much sooner than viscous dissipation in the film, $\alpha \gtrsim 90^\circ$ and $\psi < 1$, in a consistent manner with the observed inward orientation of the crown. Both the jet protrusion and crown folding induce additional mixing compared to the sole retraction of the crown of scenario B. The liquid falling back into the film after the end of the initial impact indeed seems to expand the mixed area as R_{eq} becomes larger. Consistently with the red volutes surrounding the post-impact red spot in the film, the standard deviation σ_{eq} also increases with $\delta^\star$ in scenarios C and D but at a slower rate, and the resulting concentration profile is almost uniformly distributed since $\sigma_{\mathrm{eq}}/\mathrm{Re}$ remains close to 0.45. In both scenario C and D, once $\delta^\star \gtrsim 2$, the ejected proportion φ_{e} approaches the same stationary value of about 0.6, i.e., some liquid from the drop is added in the film locally. The proportion of the drop left in the film post-impact, $\varphi_{\mathrm{d \to f'}}$, also seems to reach a limit value of about 0.5 when $\delta^\star \gtrsim 2$. This bound could possibly result from the truncation of the images at very large film thickness. Nevertheless, although $\varphi_{\mathrm{d \to f'}}$ might further increase with $\delta^\star$ in reality, it does not seem to get close to 1 for very large film thicknesses. The ejections produced by a drop impacting a liquid film thus seem to always contain liquid initially from the drop in a significant proportion. On the other hand, the ratio of the volume originating from the film and ejected away at impact, over the initial drop volume, $\varphi_{\mathrm{f \to e}}$, remains close to 0.1 once $\delta^\star \gtrsim 1$. Hence, in a consistent manner with the other observations, very little liquid coming from the film is ejected away.

The Weber number also affects crown geometry parameters, mostly in the case of scenarios C and D. In particular, a higher We results in a much higher crown, as shown in Fig. 7 (c). Correspondingly, large differences are observed between scenarios C and D in the crown shape factor ψ and the ratio of the retraction velocity components ξ (Figs 8 (b) and (c)). The ratio of velocity components is notably representative of the different mechanisms involved during the retraction phase of these two scenarios. Unlike the crown geometry parameters, the mixing level indicators (R_{eq}, σ_{eq}, φ_{e}, $\varphi_{\mathrm{d \to f'}}$ and $\varphi_{\mathrm{f \to e}}$) do not significantly vary with We. Specifically, the ejected volume should mostly depend on the first stages of the impact, i.e., the crushing of the drop in the film and the crown growth. Since the crowns observed in scenarios C and D present different geometries, it is therefore surprising to observe similar values of φ_{e} in both cases once $\delta^\star \gtrsim 2$.

The relatively minor influence of We is in contrast with the dynamics of drop impact on a dry wall, in which case the splashing threshold or maximum extension of the radius formed at impact depend strongly on We [44, 45]. This radius is also much larger than the equivalent red spot radius obtained in scenario A ($\delta^\star < 1$) [43–45]. Nevertheless, retraction and expansion strokes are also observed for impacts on a dry wall [1, 2, 44], and the final size of the spot left by the drop on the wall is usually smaller than R_{dry}, i.e., this final size and the value for R_{eq} as $\delta^\star \to 0$ might be expected to become very close. The major difference in our experiments is the presence of the initial liquid film which decreases the viscous forces acting to slow the motion of the growing crown during the impact. All our experiments also lie within regimes where $t_{\mathrm{i}} < t_{\nu}$. The case where $t_{\mathrm{i}} \approx t_{\nu}$ corresponds to a film thickness $\delta^\star = 0.15$ (18 µm) at We $= 500$ and $\delta^\star = 0.23$ (26 µm) at We $= 3000$, i.e., a range that we could not explore, but that was partly described by Yarin Weiss [64] (Fig. 12).

In Table I, we report the various correlation coefficients computed between the mixing level indicators (R_{eq}, σ_{eq}, φ_{e}, $\varphi_{\mathrm{d \to f'}}$ and $\varphi_{\mathrm{f \to e}}$) and the crown geometry parameters (α, $r_{\mathrm{t}}/r_{\mathrm{c}}$ and h). As a comparison, the correlation coefficients with $\delta^\star$ are added in the last column. We observe that the red spot radius and second-order moment, R_{eq} and σ_{eq}, along with the proportion of the drop left in the film post-impact, $\varphi_{\mathrm{d \to f'}}$, overall increase with increasing crown inclination α and decreasing ratio of the top and bottom crown radii $r_{\mathrm{t}}/r_{\mathrm{c}}$, still in accordance with the previous discussion. Indeed, a very inclined crown wall typically leads to early fragmentation and a small red spot containing very little water coming from the drop, while for $\alpha > 90^\circ$ and $r_{\mathrm{t}}/r_{\mathrm{c}} < 1$, the longer lifetime of the crown allows the mixing between the drop and the film to last longer and to occur on a larger area. It is thus also not surprising to see that these mixing level indicators are not strongly correlated to the height of the crown. Conversely, the ejected proportion φ_{e} decreases as α increases, and increases with $r_{\mathrm{t}}/r_{\mathrm{c}}$. A very inclined crown indeed allows the ejections to actually leave the impacted zone and not to fall back into the film after the impact. The proportion of volume initially in the film and ejected away at impact, $\varphi_{\mathrm{f \to e}}$, was found to remain almost constant (see Fig. 13 (b)), and is also observed to vary only little with the crown geometry parameters.

Besides the rapid expansion and retraction of the crown, the impact is also responsible for the emergence of waves at the free surface of the film, or even directly in the crown in scenarios C and D. According to Ersoy and Eslamian [39], capillary waves should participate in the mixing between the drop and the film. Measurements based on our movies yield wavelengths of 1.62 ± 0.05 mm (average ± s.d. on 49 experiments for which $\delta^\star \gtrsim 1.3$, see Supplementary Material), similarly to their findings. Capillary waves should be emitted as soon as the drop has crushed and the crown starts growing [2, 39], although they were not visible in Fig. 5 (a). The local Capillary number in the film during the first stages of the impact is $\mathrm{Ca} = \nu \rho \dot{r}_{\mathrm{c}}/\gamma$, with $\dot{r}_{\mathrm{c}}$ the edge velocity of the radially expanding cavity in the film, in this case measured for $t < t_{\mathrm{c}}$. In scenario A for very thin films at high We, $\dot{r}_{\mathrm{c}} \sim$ 1-2 m s^{-1}. From Jalaal et al. [65], based on a linear analysis of the lubrication theory we may estimate the wavelength of capillary waves in a thin viscous film of thickness $\delta^\star = 0.75$ as $\lambda \simeq 5.03\delta/\mathrm{Ca}^{1/3} = 1.6\,\mathrm{mm}$ [39, 66]. According to the lubrication equation, the exponentially decaying ripples in the film have a damping time of about $t_{\mathrm{d}} = 3\mu\lambda^4/(16\pi^4\delta^3\gamma) = 0.2\,\mathrm{ms}$, i.e., much smaller than the total crown formation and break-up timescale of a few milliseconds, and of the same order as our frame period of 0.16 ms. In scenario B, e.g., for $\delta^\star \gtrsim 1$, at We $= 2750$, the crown wall expands at a velocity of about $\dot{r}_{\mathrm{c}} \simeq 0.5\,\mathrm{m\,s^{-1}}$. The damping characteristic time of the capillary ripples t_{d} is in this case of the order of 2 ms. The capillary ripples thus also fade away before the other phenomena at play may even interact with them, and may help dissipate the remaining kinetic energy of the crown after it starts to retract toward the center. However, in the case of scenarios C and D, e.g., for $\delta^\star = 2$, the crown wall moves at a smaller velocity $\dot{r}_c \simeq 0.05-0.1\,\mathrm{m\,s^{-1}}$, yielding a damping time of the capillary ripples $t_d \in [25\,;100]$ms, which is comprised between t_c and t_V. During the last stages of the impact in particular, these capillary ripples could help dissipate the kinetic energy of any secondary droplet or blob of liquid that falls back into the film following the retraction phase of the crown. These waves could thus be more likely to prevent any further expansion of the spot left by the drop in the film following the impact, rather than to enlarge the size of the spot. This would be consistent with the observation that σ_{eq}/R_{eq} does not vary significantly between scenarios B, C and D.

VI. CONCLUSION

The progressive filling of a thin film by successive droplets of miscible liquid is a commonly encountered phenomenon [2], a particular applicative context being the growth of stalagmites in karstic caves. However, few studies are concerned with the hydrodynamics at play when drops impact thin films [27, 35], especially regarding the mixing that may occur both between the drop and the film, and into the ejections typically produced by these impacts [39]. Getting a deeper insight into the variations of ion distribution at the timescale of single drop impacts would nevertheless allow to better comprehend the growth of stalagmites and the potential differences that they exhibit in terms of, e.g., shape and size. We thus investigated in this paper the impact of a drop on a very thin film in a laboratory setting with the aim of determining how the drop content is distributed into the film upon impact. We varied the Weber number We and non-dimensional film thickness $\delta^\star$ in a range close to what is observed in actual caves. We identified several impact scenarios depending on these parameters, going from a very inclined and rapidly growing crown that fragments early to a short, slow and thick crown that produces an uprising central jet lately. The distribution of these scenarios sheds light on the influence of We and $\delta^\star$ on the final outcome of the impacts. All the measured quantities are strongly correlated to the initial film thickness $\delta^\star$. Part of them (crown geometry parameters and ejected proportion) were further corroborated or completed by data from the literature in ranges close to ours. On the other hand, only some crown geometry parameters such as the maximum height, shape and retraction velocity depend on We. Additionally, most of the mixing level indicators, such as the red spot radius and ejected proportion, are strongly correlated to the crown inclination and spatial extent.

In particular, the mixing level indicators between the drop and the film that we introduced depend mostly on $\delta^\star$ and not significantly on We. Both the equivalent radius of the spot left by the drop R_{eq} and the corresponding second-order moment σ_{eq} increase with $\delta^\star$ in the first two scenarios due to the transition from a crown fragmenting and disappearing in scenario A to a crown retracting and collapsing in a random manner for B. For scenarios C and D, R_{eq} and σ_{eq} seem to reach stationary values as the crown retraction dynamics (jet appearance or folding) enhances the spreading of the crushed drop in the film even more. The lack of influence of We on the equivalent radius is opposed to what is observed for impacts on dry walls. The ejected proportion φ_e first takes a more or less constant value of about 1 in scenario A, i.e., as much volume as brought by the drop is ejected away during the impact, no matter whether it came from the drop or the initial film. Then this proportion decreases for scenario B, meaning that a certain part of the drop volume is added to the film following the impact, increasing the thickness locally. The ejected proportion finally reaches a stationary value at large film thickness in scenarios C and D, despite the differences exhibited in the shape and retraction velocity ratio of the crown in these two cases. The proportion of the initial drop remaining in the film following the impact $\varphi_{d\to f'}$ overall increases with the film thickness in a consistent manner with the observations of the various scenarios.

All these measurements indicate that the film thickness directly influences the distribution of red in the film following the impact, as well as the volume and concentration of the droplets that are ejected away. Translated to caves, this would mean that the ion distribution in the residual water film covering stalagmites varies from one impact to the other depending on the film thickness, and so would the precipitation and accumulation of these ions and subsequent stalagmite growth. Accordingly, the film thickness seems to be locally affected by each impact. Although this thickness was thought to remain constant and uniform on actual stalagmites, such measurements added to the dispersal in the impact point position of the drops show that it should not be the case. The film thickness could still display more uniformity in between impacts separated by long periods of time ($\gtrsim 15\,$min) because of the other phenomena at play, such as the gravity-driven drainage of this film. Therefore, concluding regarding the direct influence of one drop impact on subsequent stalagmite growth is not possible without considering drainage and precipitation. This work nevertheless showed that considering a constant film thickness over time and space in attempting to model stalagmite growth is not always an hypothesis that should be made. To further study the influence of a succession of impacts on stalagmite shape, important steps would include the analysis of the interaction between drop impacts localized close to each other in a short period of time ($\sim$ 1-100 s), or the assessment of the influence of a film thickness gradient on the spot left by one drop impact.

ACKNOWLEDGEMENT

The authors gratefully thank Olivier Verlaine (University of Liège) for the use of the spectrometer, and Loïc Tadrist (Aix-Marseille University) for fruitful discussion and advice regarding the experimental setup.

Appendix A: Nomenclature

TABLE II. List of physical properties and characteristic scales and corresponding symbols, with their definition and typical values (see Section II C for variable definitions).

SYMBOL	VALUE/RANGE	UNITS	DESCRIPTION
	Water physical properties		
ρ	1000	$\mathrm{kg\,m^{-3}}$	Density
ν	10^{-6}	$\mathrm{m^2\,s^{-1}}$	Kinematic viscosity
γ	70	$\mathrm{mN\,m^{-1}}$	Surface tension
D	$\sim 10^{-9}$	$\mathrm{m^2\,s^{-1}}$	Dye diffusion coefficient
	Characteristic scales		
	Timescales		
t_i	$[0.7\,;1.5]$	ms	Drop crushing time
t_c	15	ms	Capillary time
t_ν	$[5\,;280]$	ms	Viscous diffusion timescale over δ
$t_{\nu,\mathrm{d}}$	6	s	Viscous diffusion timescale over r_d
$t_{\downarrow/\rightarrow}$	$10/90$	s/min	Concentration homogenization timescale by vertical/horizontal diffusion
t_d	$[0.2\,;200]$	ms	Capillary ripples damping time
	Length scales		
$\delta(\delta^\star=1)$	115	µm	-
R_dry	$[12\,;18]$	mm	Maximum radius of drop impacting on dry wall
λ	1.6	mm	Capillary ripples wavelength
λ_c	2.7	mm	Capillary length
	Other		
$\dot{r}_\mathrm{c}$	$[0.05\,;1]$	$\mathrm{m\,s^{-1}}$	Cavity expansion velocity
V_f	$[10^{-7}\,;10^{-6}]$	$\mathrm{m^3}$	Film volume
	Non-dimensional numbers		
Oh	$1.7\cdot10^{-3}$	-	Ohnesorge
We	$[525\,;2750]$	-	Weber
Pe	1000	-	Péclet
$\delta^\star$	$[0.4\,;4.3]$	-	Film thickness
t_ν/t_i	$[3\,;400]$	-	Ratio of viscous diffusion and drop crushing timescales (Reynolds)

TABLE III. List of measured quantities and corresponding symbols, with their definition and typical values (see Section II A for side view variable definitions and Sections II B and IV B for top view variable definitions).

SYMBOL	VALUE/RANGE	UNITS	DESCRIPTION
Side view measurements			
Impacting drop			
r_d	2.3	mm	Radius
u_d	[2.9 ; 6.6]	$\mathrm{m\,s^{-1}}$	Velocity
Film			
δ	[65 ; 500]	µm	Thickness
Crown geometry			
α	[50 ; 105]	°	Inclination
r_t	[10 ; 20]	mm	Top radius
r_c	[8 ; 18]	mm	Cavity radius
h	[6 ; 22]	mm	Height
ψ	[−2.2 ; 1.8]	mm	Shape factor
Crown retraction			
j	[8 ; 22]	mm	Jet length
ξ	[0.3 ; 2.3]	mm	Retraction velocity ratio
Top view measurements			
Colorimetry measurements			
p_r	[0 ; 0.05]	-	Red dye proportion
p_g	0.05	-	Green dye proportion
δ_r	[0 ; 25]	µm	Red partial film thickness
δ_g	[0 ; 25]	µm	Green partial film thickness
Equivalent moments			
R_eq	[6 ; 16]	mm	Equivalent red stain radius
σ_eq	[2 ; 5]	mm	Second-order moment
Proportions			
φ_e	[0.6 ; 1]	-	Ejected volume proportion
$\varphi_{\mathrm{d}\to\mathrm{f}'}$	[0 ; 0.5]	-	Drop volume proportion left in the film
$\varphi_{\mathrm{f}\to\mathrm{e}}$	[0 ; 0.1]	-	Ejected film volume over initial drop volume ratio

Appendix B: Materials and methods

In the following sections, we go over the detailed calculations of the colorimetry measurement. We first apply Beer-Lambert law to our experimental setup and approximate the obtained equation. We also review the method used to fit the coefficients appearing therein. Finally, we show how we can retrieve the thickness and red dye proportion of a given picture based on a calibration performed beforehand.

1. Colorimetry measurement

In the following, the subscripts r and g respectively stand for the red and green dyes. The R, G and B subscripts represent the red, green and blue color channels of the camera sensor, each having values that range from 0 to 1. We consider the reflectance of light over a thin film of thickness δ containing several dyes i ($i \in \{r, g\}$) at concentrations c_i (in M). The incident light is non-polarized and normal to the water surface, with an intensity spectrum $I_0(\lambda)$. According to Fresnel equations, a fraction $\alpha I_0(\lambda)$ is reflected at the water/air interface, while the remainder $(1-\alpha)I_0(\lambda)$ is transmitted into the water. The coefficient α depends on the refraction index of water, which is relatively independent of wavelength in the visible range, so $\alpha \simeq 0.02$. The transmitted light is then partly absorbed by the dyes according to Beer-Lambert's law, so the intensity of the light impacting the bottom surface of the water film is

$$I_1(\lambda) = (1-\alpha)I_0(\lambda)\exp\left[-\delta\sum_i c_i\varepsilon_i(\lambda)\right], \tag{B1}$$

where the optical path length simply equals the film thickness δ, and ε_i represents the molar extinction coefficient of each dye in solution (in $\mathrm{M}^{-1}\,\mathrm{m}^{-1}$).

Again, only a fraction $\beta I_1(\lambda)$ of this light is reflected at the bottom of the water film. This light is once more absorbed by the film, so the intensity of the beam returning to the water/air interface is

$$I_2(\lambda) = \beta I_1(\lambda)\exp\left[-\delta\sum_i c_i\varepsilon_i(\lambda)\right]. \tag{B2}$$

Finally, a fraction $(1-\alpha)I_2(\lambda)$ crosses the water/air interface and reaches the camera. Since $\alpha \ll 1$, subsequent reflections are neglected. The light spectrum arriving onto the camera sensor is therefore

$$\left[\alpha + \beta(1-\alpha)^2\exp\left(-2\delta\sum_i c_i\varepsilon_i(\lambda)\right)\right]I_0(\lambda). \tag{B3}$$

Each sensor j of the camera ($j \in \{R, G, B\}$) will receive a signal X_j integrated over the wavelength spectrum:

$$X_j = \int_0^\infty \left[\alpha + \beta(1-\alpha)^2\exp\left(-2\delta\sum_i c_i\varepsilon_i(\lambda)\right)\right]I_0(\lambda)S_j(\lambda)\mathrm{d}\lambda, \tag{B4}$$

where $S_j(\lambda)$ is the camera spectrum, namely the sensitivity of sensor j to a given wavelength λ. From this equation, it is not possible to determine δ and c_i without knowing the spectra of incident light $I_0(\lambda)$, absorption $\varepsilon_i(\lambda)$ and camera $S_j(\lambda)$. However, in the limit where $\delta c_i\varepsilon_i \ll 1$, a Taylor series approximation of the exponential can be considered, which yields:

$$\begin{aligned} X_j &\simeq \int_0^\infty \left[\alpha + \beta(1-\alpha)^2\right]I_0(\lambda)S_j(\lambda)\mathrm{d}\lambda \\ &\quad -\sum_i \delta c_i \int_0^\infty 2\beta(1-\alpha)^2\varepsilon_i(\lambda)I_0(\lambda)S_j(\lambda)\mathrm{d}\lambda \\ &\quad +\sum_{i,k} \delta^2 c_i c_k \int_0^\infty 2\beta(1-\alpha)^2\varepsilon_i(\lambda)\varepsilon_k(\lambda)I_0(\lambda)S_j(\lambda)\mathrm{d}\lambda \\ &\quad +\mathscr{O}\left[(\delta c\varepsilon)^3 I_0 S\lambda\right] \\ &\simeq A_j - \delta\sum_i B_{ij}c_i + \delta^2\sum_{i,k} C_{ikj}c_i c_k \end{aligned} \tag{B5}$$

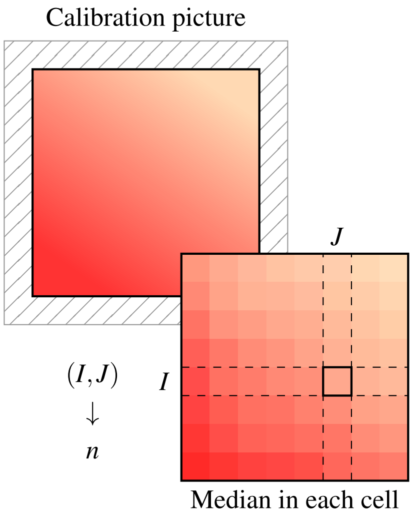

FIG. 14. Cutting of pictures in square cells and numbering.

with $C_{ikj} = C_{kij}$. In the limit where there is no film on the white substrate, i.e. $\delta = 0$, all R, G and B values observed on screen should be close to 1. In other words, the coefficients A_j can all be set to 1. Additionally, the dyes are only diluted in water and their concentrations c_i solely depend on the proportions of dye in water, defined as p_r and p_g for the red and green dyes in the film, respectively, and $p_{r,\mathrm{d}}$ the proportion of red dye in the incoming drop. The products $B_{ij}c_i$ and $C_{ikj}c_ic_k$ can thus be replaced by their non-dimensional counterparts $B'_{ij}p_i$ and $C'_{ikj}p_ip_k$, respectively.

Previous calculations hold in each point of the picture captured by the sensor only if the lighting is perfectly uniform throughout the entire film. In reality, it is not the case. There were several lamps, each of them placed in a corner of the setup and oriented as perpendicularly as possible to the underlying film, since right above this film were placed the releasing drop device as well as the camera. To take that effect into account, the (R,G,B) values can be viewed as the product of two independent contributions: the absorbance of the light by the various dyes, and the spatial non-uniformity of lighting. The film thickness and the dye proportions should also vary with the position. The three parameters (δ, p_r and p_g) are also not independent. In the case of the calibration pictures, the film thickness is measured beforehand and considered as uniform and therefore known in every position. On the other hand, in the experiments, as we used the same green proportion in both the drop and the film, whether it is prior to or after the impact, $p_g = 0.05$ everywhere (see Section II B). In any case only the products $p_i\delta$ are unknown. We therefore consider the partial thicknesses in red and green, defined as $\delta_r = p_r\delta$ and $\delta_g = p_g\delta$. The former equation thus reduces to

$$X_j(\boldsymbol{x}) = \left[1 - \sum_i B'_{ij}\delta_i(\boldsymbol{x}) + \sum_{i,k} C'_{ikj}\delta_i(\boldsymbol{x})\delta_k(\boldsymbol{x})\right]\ell_j(\boldsymbol{x})\,, \tag{B6}$$

where $\ell_j(\boldsymbol{x})$ is the factor accounting for the lighting non-uniformity relative to channel color j at position $\boldsymbol{x}$. The notation from the last relation does not imply a summation on index j.

a. Coefficient fit

The fitting parameters relative to all color channels R, G and B can be found independently from each other. As an example, we focus on the red component that we denote by a matrix $\mathbf{R} \in \mathbb{R}^{M\times N}$, whose elements are R_{mn}. To find these coefficients, $M = 175$ dyed water films of known thickness and fixed red and green proportions were photographed (see Supplementary Material) with the same color high-speed camera and lighting conditions. A 50-px wide stripe (which corresponds roughly to one and a half times the capillary length) is first removed on each side of the 512×512 px pictures in order not to see the physical edges of the tape nor the diminution of the film thickness towards zero. The picture then obtained is divided into 40×40 10-px side square cells, sorted from 1 to $N = 1600$ using the index n. The spatial median of the intensity of each color channel is taken in every cell, such that R_{mn} is the median of the red component in the n^{th} cell of the m^{th} experiment, as shown in Fig. 14. For each calibration experiment, there are actually two pictures divided in cells in which the median is computed, then the average of these medians is used in the matrix $\mathbf{R}$. The first picture is taken right after measuring the thickness of the film. Both pictures are taken when the substrate is horizontal, but the second one is taken after gently tilting the plate back and forth to avoid seeing any thickness variation that might have been caused by the needle tip entering and leaving the film.

Based on Eq. (B6), a design matrix $\mathbf{D} \in \mathbb{R}^{M\times P}$ contains partial film thicknesses for all the calibration experiments, with P the number of dye absorption coefficients stored in an unknown vector $\boldsymbol{c} \in \mathbb{R}^{P\times 1}$. Each experiment corresponds in the design matrix to the row $\begin{bmatrix}1 & \delta_r & \delta_g & \delta_r^2 & \delta_r\delta_g & \delta_g^2\end{bmatrix}$. In addition to that, we also look for a vector $\boldsymbol{\ell} \in \mathbb{R}^{N\times 1}$ that accounts for the spatial lighting non-uniformity. In the case of the red channel, the fitting vectors are written as

$$\boldsymbol{c} = \begin{bmatrix} 1 \\ -B_{rR} \\ -B_{gR} \\ C_{rrR} \\ 2C_{rgR} \\ C_{ggR} \end{bmatrix} \quad \text{and} \quad \boldsymbol{\ell} = \begin{bmatrix} \ell_{1,R} \\ \\ \vdots \\ \\ \ell_{N,R} \end{bmatrix} .$$

We aim at finding the $(P+N)$ unknown coefficients that minimize the objective function

$$\mathbf{E} = \mathbf{R} - \mathbf{D}\boldsymbol{c}\boldsymbol{\ell}^T \approx \mathbf{0} \tag{B7}$$

in the least square sense. This may be achieved by minimizing the sum of the residuals $\mathscr{R}$ which corresponds to the Froebenius matrix norm of the former expression, or its square for the sake of simplicity:

$$\boldsymbol{c}, \boldsymbol{\ell}: \ \min_{\boldsymbol{c},\boldsymbol{\ell}} \mathscr{R}^2 = \min_{\boldsymbol{c},\boldsymbol{\ell}} \operatorname{tr}\left(\mathbf{E}^T\mathbf{E}\right) . \tag{B8}$$

Cancelling the derivatives of $\mathscr{R}^2$ with respect to $\boldsymbol{c}$ and $\boldsymbol{\ell}$ each give a set of P and N equations:

$$\partial_{\boldsymbol{c}}\mathscr{R}^2 = \mathbf{D}^T\mathbf{R}\boldsymbol{\ell} - \boldsymbol{\ell}^T\boldsymbol{\ell}\mathbf{D}^T\mathbf{D}\boldsymbol{c} = \mathbf{0}, \tag{B9}$$

$$\partial_{\boldsymbol{\ell}}\mathscr{R}^2 = \mathbf{R}^T\mathbf{D}\boldsymbol{c} - \boldsymbol{c}^T\mathbf{D}^T\mathbf{D}\boldsymbol{c}\boldsymbol{\ell} = \mathbf{0}. \tag{B10}$$

To solve these equations for $\boldsymbol{c}$, $\boldsymbol{\ell}$, Newton-Raphson method is applied, in which case we denote by $\boldsymbol{x}^k$ the root vector at iteration k and $\boldsymbol{f}$ the set of functions:

$$\boldsymbol{x}^k = \begin{bmatrix} \boldsymbol{c} \\ \boldsymbol{\ell} \end{bmatrix}^k , \quad \boldsymbol{f} = \begin{bmatrix} \partial_{\boldsymbol{c}}\mathscr{R}^2 \\ \partial_{\boldsymbol{\ell}}\mathscr{R}^2 \end{bmatrix} . \tag{B11}$$

The corresponding Jacobian matrix is given by

$$\mathbf{J} = \left[\begin{array}{c|c} -\boldsymbol{\ell}^T\boldsymbol{\ell}\mathbf{D}^T\mathbf{D} & \mathbf{D}^T\mathbf{R} - 2\mathbf{D}^T\mathbf{D}\boldsymbol{c}\boldsymbol{\ell}^T \\ \hline \mathbf{R}^T\mathbf{D} - 2\boldsymbol{\ell}\boldsymbol{c}^T\mathbf{D}^T\mathbf{D} & -\boldsymbol{c}^T\mathbf{D}^T\mathbf{D}\boldsymbol{c}\mathbb{I} \end{array}\right] . \tag{B12}$$

At the $(k+1)^{\text{th}}$ iteration, we have $\boldsymbol{x}^{k+1} = \boldsymbol{x}^k - \mathbf{J}^{-1}(\boldsymbol{x}^k)\boldsymbol{f}(\boldsymbol{x}^k)$, with all elements of $\boldsymbol{x}^0$ initialized to 1. The unknowns are indeed for the most part lighting variation coefficients that should be close to 1. Convergence is attained once the norm of the error between two iterates, $\left\|\boldsymbol{x}^{k+1} - \boldsymbol{x}^k\right\|$, goes below an arbitrary threshold of 10^{-3}.

b. Coefficient values

The coefficients representing the dye absorption and found with the calibration technique described here above are shown in Table IV, for the three color channels. Despite the difference between their orders of magnitude, the series from Eq. (B6) converge. As an example, we may consider the on-screen color variations in a point of a 100 µm-thick film containing red and green dyes both in proportions of 0.05. The variations due to, e.g., B_{gR} and B_{gG} would be respectively of $B_{gR}\,p_r\,\delta^\star = 7 \times 0.05 \times 0.86 = 0.30$ and $B_{gG}\,p_g\,\delta^\star = 0.06$. Since they appear in Eq. (B6) as decrements from 1, adding green in the film expectedly induces a larger variation to the red component than to the green one, yet they are both in the same range of values. For, e.g., a very thin film ($\delta^\star \ll 1$) containing only green dye, the green component would be almost 1. Additionally, the lighting spatial variations represented by the $\boldsymbol{\ell}$ vector from Eq. (B6) are shown in Figs 15 (a-c), for all three color channels. It can be seen

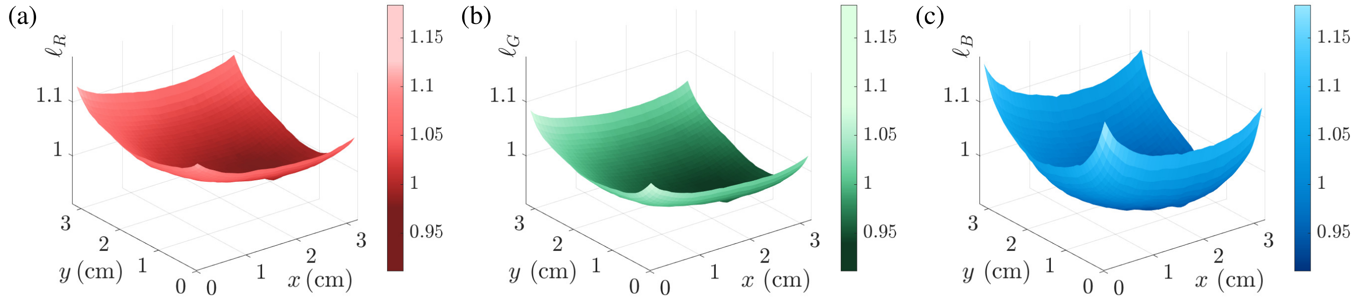

FIG. 15. Lighting coefficients $\ell_j(\boldsymbol{x})$ relative to Eq. (B6), for (a) $j = R$, (b) $j = G$ and (c) $j = B$. Coefficients were obtained by solving Eq. (B7) in the least-square sense with a Newton-Raphson technique.

that for a given j value, the light exposure is greater in the corners, whilst it decreases towards the center of the picture. This is due to the four lamps placed in the corners of the experimental setup. The camera sensor has a less intense, broader spectral response to the blue color than to the red and green, which translates into Fig. 15 (c) by sharper variations around the edges.

TABLE IV. Absorption coefficients from $\boldsymbol{c}$ relative to Eq. (B6), for all three color channels. Coefficients were obtained by solving Eq. (B7) in the least-square sense with a Newton-Raphson technique.

j	B_{rj}	B_{gj}	C_{rrj}	C_{rgj}	C_{ggj}
R	0.1	7.0	-6.2	-3.1	20.7
G	12.9	1.4	61.5	13.6	3.0
B	11.8	7.7	67.9	19.2	49.1

2. Retrieving the thickness and concentration in an arbitrary picture

Using the color and lighting coefficients found with the calibration pictures, two out of the three parameters (film thickness, proportions of red and green dyes) can be retrieved based on an arbitrary picture. As aforementioned, before the impact the film had a uniform thickness and green proportion always fixed to $p_g = 0.05$. The impacting drop contained both red and green dyes of known proportions $p_{r,\mathrm{d}}$ and p_g, the latter having the same value as in the film. After the impact the green dye proportion is therefore known everywhere in the film. Computing the post-impact film thickness and red proportion in each point allows to assess how the drop and the film are mixing directly after impact.

To do so, we proceed in the same manner as for the calibration and first divide the post-impact picture of the film in 40 × 40 10-px side square cells, in which the median of red, green and blue components are computed. Focusing once again on the red component, we therefore get a vector $\boldsymbol{r} \in \mathbb{R}^{N\times 1}$ containing all the red values of the N cells into which the picture was divided. The unknown is this time the matrix $\mathbf{D} \in \mathbb{R}^{N\times P}$ where each row $\begin{bmatrix} 1 & \delta_r & \delta_g & \delta_r^2 & \delta_r\delta_g & \delta_g^2 \end{bmatrix}$ corresponds no longer to the average values taken by the partial thicknesses in a given experiment, but to the partial thicknesses in a given point of the film. We aim at solving the following equation:

$$\boldsymbol{r} = \mathbf{L}\mathbf{D}\boldsymbol{c}, \tag{B13}$$

with $\mathbf{L} \in \mathbb{R}^{N\times N}$ the diagonal matrix containing all the values from vector $\boldsymbol{\ell}$. As the system is non-linear with respect to the partial film thicknesses, it cannot be solved directly, nor for the entire picture at once, and computations should be made independently for all cells. To find the values of δ_r, δ_g in each case n of the discretized picture, we proceed by applying once again the Newton-Raphson technique. In this case we look in each cell n of the picture for the unknown vector $\boldsymbol{x}_n = \begin{bmatrix} \delta_{r,n} & \delta_{g,n} \end{bmatrix}^T$ with $\delta_{i,n}$ the partial film thickness in the n^{th} cell. We also rewrite and cancel Eq. (B6) such that it becomes the set of functions $f_{j,n}$ to solve:

$$f_{j,n} = \left(1 - \frac{X_{jn}}{\ell_{jn}}\right) - \sum_i B_{ij}\delta_{i,n} + \sum_{i,k} C_{ikj}\delta_{i,n}\delta_{k,n} = 0\,. \tag{B14}$$

The derivatives of $f_{j,n}$ with unknowns $\delta_{i,n}$, which correspond to the Jacobian matrix element $J_{ji,n}$, are given by

$$J_{ji,n} = -B_{ij} + 2\sum_k C_{ikj}\delta_{k,n}\,. \tag{B15}$$

Since there are three color channels and two unknowns, the Jacobian $\mathbf{J}_n$ in each cell is a (3×2) matrix that we use to compute the vector $\boldsymbol{x}_n^{k+1}$ at the $(k+1)^{th}$ iteration as follows: $\boldsymbol{x}_n^{k+1} = \boldsymbol{x}_n^k - \mathbf{J}_n^+(\boldsymbol{x}^k)\,\boldsymbol{f}_n(\boldsymbol{x}^k)$, with $\mathbf{J}_n^+ = \left(\mathbf{J}_n^T\mathbf{J}_n\right)^{-1}\mathbf{J}_n^T$.

The error is computed as the absolute difference between two consecutive iterates of the vector containing all $\boldsymbol{x}_n$, defined as $\boldsymbol{X}^k = \begin{bmatrix} \boldsymbol{x}_1^k \\ \vdots \\ \boldsymbol{x}_N^k \end{bmatrix} \in \mathbb{R}^{(2N\times 1)}$, namely $\left|\boldsymbol{X}^{(k+1)} - \boldsymbol{X}^k\right|$. Convergence is reached out when this error goes below an arbitrary threshold of 10^{-3}, which typically occurs after about 5 iterations.

3. Checking the hypotheses underlying the colorimetry measurement

a. Thickness variation of a thin film on a planar substrate

Mechanical thickness measurements were mostly taken close to the center of the film because of the strong curvature exhibited by the film interface toward the edges of the substrate. Due to this curvature, spatial variations also appear to be greater in the colorimetry measurements. We may verify over which spatial extent does a thin film keep a thickness close to its maximum thickness $\delta_0 = 100\,\mu\text{m}$. We assume that the film lies on a horizontal substrate of side $W = 40\,\text{mm}$ and has a symmetric shape. In two dimensions, the liquid/air interface of the film can be modelled using the Young-Laplace equation [66]:

$$\rho g \delta(x) - \gamma \frac{\mathrm{d}^2\delta}{\mathrm{d}x^2} = K\,, \tag{B16}$$

where K is a constant pressure jump. The boundary conditions are $\delta(0) = \delta_0$ and $\delta(W/2) = \delta(-W/2) = 0\,\mu\text{m}$. Introducing the capillary length $\lambda_\text{c} = \sqrt{\gamma/(\rho g)} = 2.73\,\text{mm} \ll W$, we find that the solution to the former equation reduces to

$$\delta(x) = \delta_0\left(1 - \frac{\cosh(x/\lambda_\text{c})}{\sinh(W/(2\lambda_\text{c}))}\right)\,. \tag{B17}$$

The distance from the center over which the film thickness is decreased by 3 % is 1.04 cm. On the other hand, after a distance of 1.5 cm, the film thickness only reaches 84 % of δ_0. It is therefore not surprising for the colorimetry measurement technique to produce the spatial variations shown in, e.g., Fig. 3 (c), nor to get differences between average manual and colorimetry measurements, as shown in the graph of Fig. 4 (a).

b. Verification of the hypothesis made on $\delta c_i \varepsilon_i$

In approximating the exponential from Beer-Lambert's law by a Taylor series (see Eq. (B5)), we assumed that $\delta c_i \varepsilon_i \ll 1$ was true for all the dyes used (red, yellow and blue). We verify this hypothesis in the present section. The following calculations are made using $\delta = 100\ \mu\text{m}\ \forall i,\ i \in \{r,y,b\}$. In the impact experiments, proportions of red and green $p_{r,\text{d}} = p_g = 0.05$ were used. These correspond to actual concentrations $c_r = 1038\,\mu\text{M}$, $c_y = 524\,\mu\text{M}$ and $c_b = 106\,\mu\text{M}$ in the drop and the film as measured by a spectrometer. The molar extinction coefficients of the dyes at their respective absorption peak wavelengths are $\varepsilon_r(516\,\text{nm}) = 20097\,\text{M}^{-1}\,\text{cm}^{-1}$, $\varepsilon_y(428\,\text{nm}) = 22974\,\text{M}^{-1}\,\text{cm}^{-1}$ and $\varepsilon_b(630\,\text{nm}) = 100661\,\text{M}^{-1}\,\text{cm}^{-1}$ [67–69]. We thus obtain that $\delta c_r \varepsilon_r = 0.21$, $\delta c_y \varepsilon_y = 0.12$ and $\delta c_b \varepsilon_b = 0.11$, i.e., these values are all $\ll 1$. For films with thicknesses larger than 500 µm we would not longer be able to apply the algorithm as we would get $\delta c_r \varepsilon_r \to 1$, hence the upper limit of the range considered here.

4. Substrate area and dismissed experiments

The tape on which the liquid film was spread out has an average side of about 40 mm. A cavity formed in the film reaching a maximum radius r_c of about 10-15 mm should therefore not interact with the edges of this substrate. For larger film thicknesses ($\delta^\star \gtrsim 2$), the maximum radius r_c may be closer to 20 mm. Hence, larger tapes of sides close to 55-60 mm were used in this case

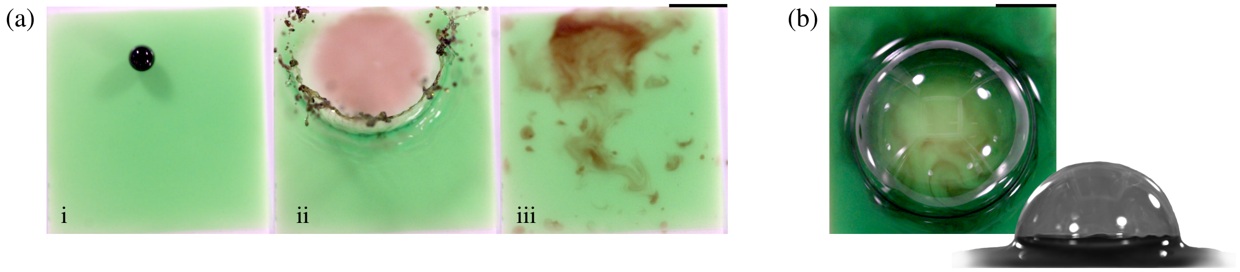

FIG. 16. Possible rejected experiments: (a) Impact occurring too close to an edge, in this case at a distance of 8 mm of the upper border of the film in the field of view. The parameters are $\delta^\star = 1.3$ and $\mathrm{We} = 2750$. The maximum radius r_c of the cavity in the film is 13 mm. (b) Air entrapment in the case of an impact for which $\delta^\star = 4.3$ and $\mathrm{We} = 1675$. The scale bars are 1 cm.

but the field of view remained the same as it did not prevent to see the crown expansion dynamics. However, the limited area of the film could still possibly affect the impact in two cases: i) if the drop were to land too close to an edge, ii) if capillary waves reflecting on the film outer borders were interacting with the developing cavity or during the retraction phase. In the first case, it would not be surprising that the crown behaviour changes in response to an impact that would occur at less than one times the maximum r_c value from the edge. This may be seen in Fig. 16 (a) for $\delta^\star = 1.3$ and $\mathrm{We} = 2750$ where the impact point is located at 8 mm from the closest border (Fig. 16 (a) i), while the maximum value of r_c in this range is typically of 13 mm. The crown partially breaks up when it meets the edge (Fig. 16 (a) ii). The remaining part of the crown is expelled in the opposite direction in an asymmetric manner, creating an elongated post-impact mixing pattern in the film (Fig. 16 (a) iii). As the trajectory of the drop free fall is protected from parasitic air currents, such kinds of impacts only arise when the falling height becomes sufficient for the drop to be self-deviated [24], in this case above 3 m of fall, or for $\mathrm{We} \gtrsim 2000$. Whenever this issue was encountered, corresponding data were therefore not taken into account.

The reflection of capillary waves should not affect the impact dynamics either. As aforementioned the tape size is chosen to ensure that there is at least a 10 mm space around the crown at its maximum extension. The velocities $\dot{r}_\mathrm{c}$ take values comprised between roughly $1\,\mathrm{m\,s^{-1}}$ and $0.1\,\mathrm{m\,s^{-1}}$ (see Section V). A capillary wave front propagating at the same celerity [65] would need respectively 20 ms and 200 ms to cover a distance of 10 mm back and forth. These two bounds correspond to scenarios A and D, for which capillary ripples have respective damping times of the order of 0.3 ms and 30 ms (for, e.g., $\delta^\star = 0.5$ and $\delta^\star = 2.5$). These ripples would therefore fade away before having the chance to interact with the crown. Another cause, although rarely observed, for dismissing experiments from scenario D is the possible entrapment of an air bubble due to the crown folding upon itself. An example is shown in Fig. 16 (b) in the case of a vary large bubble, having a 13 mm radius. The bubble having a lifetime of several seconds prevents the underneath final mixing pattern to be analyzed as it cannot be seen in the final frame of the movie, whose duration is only about 1 s.

---

[1] M. Rein, Phenomena of liquid drop impact on solid and liquid surfaces, Fluid Dyn. Res. **12**, 61 (1993).
[2] A. L. Yarin, Drop impact dynamics: splashing, spreading, receding, boucing, . . ., Annu. Rev. Fluid Mech. **38**, 159 (2006).
[3] J. Breitenbach, I. Roisman, and C. Tropea, From drop impact physics to spray cooling models: a critical review, Exp. Fluids **59**, https://doi.org/10.1007/s00348-018-2514-3 (2018).
[4] Q. Liu and M. Orme, High precision solder droplet printing technology and the state-of-the-art, J. Mater. Process. Tech. **115**, 271 (2001).
[5] C. Vernay, L. Ramos, J.-P.Douzals, R. Goyal, J.-C. Castaing, and C. Ligoure, Drop impact experiment as a model experiment to investigate the role of oil-in-water emulsions in controlling the drop size distribution of an agricultural spray, Atomization Spray **26**, https://doi.org/10.1615/AtomizSpr.2015013630 (2016).
[6] L. Deike, Mass transfer at the ocean–atmosphere interface: The role of wave breaking, droplets, and bubbles, Annu. Rev. Fluid Mech. **54**, 191 (2022).
[7] Y. Joung and C. Buie, Aerosol generation by raindrop impact on soil, Nat. Commun. **6**, https://doi.org/10.1038/ncomms7083 (2015).
[8] A. Baker, C. L. Smith, C. Jex, I. J. Fairchild, D. Genty, and L. Fuller, *Annually Laminated Speleothems: a Review*, Vol. 37 (2008) pp. 193–206.
[9] A. Baker, D. Genty, W. Dreybrodt, W. L.Barnes, N. J. Mockler, and J. Grapes, Testing theoretically predicted stalagmite growth rate with recent annually laminated samples: implications for past stalagmite deposition, Geochim. Cosmochim. Ac. **62**, 393 (1998).

[10] T. Gilet and L. Bourouiba, Fluid fragmentation shapes rain-induced foliar disease transmission, J. R. Soc. Interface **12**, https://doi.org/10.1098/rsif.2014.1092 (2015).

[11] S. Lejeune, T. Gilet, and L. Bourouiba, Edge effect: Liquid sheet and droplets formed by drop impact close to an edge, Phys. Rev. Fluids **3**, https://doi.org/10.1103/PhysRevFluids.3.083601 (2018).

[12] S. Lejeune and T. Gilet, Drop impact close to the edge of an inclined substrate:liquid sheet formation and breakup, Phys. Rev. Fluids **4**, https://doi.org/10.1103/PhysRevFluids.4.053601 (2019).

[13] W. Dreybrodt, *Processes in Karst Systems* (Springer series in physical environment, 1988).

[14] D. Buhmann and W. Dreybrodt, The kinetics of calcite dissolution and precipitation in geologically relevant situations of karst areas: 1. open system, Chem. Geol. **48**, 189 (1985).

[15] W. Dreybrodt, Chemical kinetics, speleothem growth and climate, Boreas **28**, 347 (1999).

[16] M. Tan, A. Baker, D. Genty, C. SMith, J. Esperd, and B. Cai, Applications of stalagmite laminae to paleoclimate reconstructions: Comparison with dendrochronology/climatology, Quaternary Sci. Rev. **25**, https://doi.org/10.1016/j.quascirev.2006.01.034 (2006).

[17] I. Labuhn, D. Genty, H. Vonhof, C. Bourdin, D. Blamart, E. Douville, J. Ruan, H. Cheng, R. L. Edwards, E. Pons-Branchu, and M. Pierre, A high-resolution fluid inclusion δ180 record from a stalagmite in sw france: modern calibration and comparison with multiple proxies, Quaternary Sci. Rev. **110**, 152 (2015).

[18] Y. A. Brahim, M. C. Peros, A. E. Viau, M. Liedtke, J. M. Pajón, J. Valdes, R. L. E. X. Li, E. G. Reinhardt, and F. Oliva, Hydroclimate variability in the caribbean during north atlantic heinrich cooling events (h8 and h9), Sci. Rep.-UK **12**, https://doi.org//10.1038/s41598-022-24610-x (2022).

[19] J. Baldini, Cave atmosphere controls on stalagmite growth rate and palaeoclimate records, Geological Society, London, Special Publications **336**, 283 (2010).

[20] D. Genty, A. Baker, and B. Vokal, Intra- and inter-annual growth rate of modern stalagmites, Chem. Geol. **176**, 191 (2001).

[21] J. U. L. Baldini, F. A. Lechleitner, S. F. M. Breitenbach, J. van Hunen, L. M. Baldini, P. M. Wynn, R. A. Jamieson, H. E. Ridley, A. J. Baker, I. W. Walczak, and J. Fohlmeister, Detecting and quantifying palaeoseasonality in stalagmites using geochemical and modelling approaches, Quaternary Sci. Rev. **254**, 106784 (2021).

[22] E. Nakouzi, R. E. Goldstein, and O. Steinbock, Do dissolving objects converge to a universal shape, Langmuir **31**, 4145 (2015).

[23] W. Dreybrodt, Evolution of the isotopic composition of carbon and oxygen in a calcite precipitating h_2o–co_2–$caco_3$ solution and the related isotopic composition of calcite in stalagmites, Geochim. Cosmochim. Ac. **72**, 4712 (2008).

[24] J. Parmentier, S. Lejeune, M. Maréchal, F. Bourges, D. Genty, V. Terrapon, J.-C. Maréchal, and T. Gilet, A drop does not fall in a straight line: a rationale for the width of stalagmites **475**, http://doi.org/10.1098/rspa.2019.0556 (2019).

[25] E. Reyssat, F. Chevy, A.-L. Biance, L. Petitjean, and D. Quéré, Shape and instability of free-falling liquid globules, Europhys. Lett. **80**, https://doi.org/10.1209/0295-5075/80/34005 (2007).

[26] E. Villermaux and B. Bossa, Single-drop fragmentation determines size distribution of raindrops, Nat. Phys. **5**, 697– (2009).

[27] A.-B. Wang and C.-C. Chen, Splashing impact of a single drop onto very thin liquid films, Phys. Fluids **12**, 2155 (2000).

[28] G. E. Cossali, M. Marengo, A. Coghe, and S. Zhdanov, The role of time in single drop splash on thin film, Exp. Fluids **36**, 888 (2004).

[29] Z. Levin and P. V. Hobbs, Splashing of water drops on solid and wetted surfaces: Hydrodynamics and charge separation, Philos. T. R. Soc. S.-A **269**, 555 (1971).

[30] L. V. Zhang, P. Brunet, J. Eggers, and R. D. Deegan, Wavelength selection in the crown splash, Phys. Fluids **22**, https://doi.org/10.1063/1.35267435 (2010).

[31] I. V. Roisman and C. Tropea, Impact of a drop onto a wetted wall: description of crown formation and propagation, J. Fluid Mech. **472**, 373 (2002).

[32] C. Josserand, P. Ray, and S. Zaleski, Droplet impact on a thin liquid film: anatomy of the splash, J. Fluid Mech. **802**, 775 (2016).

[33] G. E. Cossali, A. Coghe, and M. Marengo, The impact of a single drop on a wetted solid surface, Exp. Fluids **22**, 463 (1997).

[34] R. Rioboo, C. Bauthier, J. Conti, M. Voué, and J. D. Coninck, Experimental investigation of splash and crown formation during single drop impact on wetted surfaces, Exp. Fluids **35**, 648 (2003).

[35] A. I. Fedorchenko and A.-B. Wang, On some common features of drop impact on liquid surfaces, Phys. Fluids **16**, 1349 (2004).

[36] M. Beczek, M. Ryżak, A. Sochan, R. Mazur, C. Polakowski, and A. Bieganowski, The differences in crown formation during the splash on the thin water layers formed on the saturated soil surface and model surface, PloS One **12**, https://doi.org/10.1371/journal.pone.0181974 (2017).

[37] N. Chen, H. Chen, and A. Amirfazli, Drop impact onto a thin film: Miscibility effect, Phys. Fluids **29**, https://doi.org/10.1063/1.5001743 (2017).

[38] H. M. Kittel, I. V. Roisman, and C. Tropea, Splash of a drop impacting onto a solid substrate wetted by a thin film of another liquid, Phys. Rev. Fluids **3**, https://doi.org/10.1103/PhysRevFluids.3.073601 (2018).

[39] N. E. Ersoy and M. Eslamian, Capillary surface waves formation and mixing of miscible liquids during drop impact onto a liquid film, Phys. Fluids **31**, https://doi.org/10.1063/1.5064640 (2019).

[40] E. Villermaux and B. Bossa, Drop framgentation on impact, J. Fluid Mech. **668**, 412 (2011).

[41] F. P. Incropera, D. P. DeWitt, T. L. Bergman, and A. S. Lavine, Incropera's principles of heat and mass transfer https://doi.org/10.1007/s00348-018-2514-3 (2017).

[42] A. L. N. Moreira, A. S. Moita, and M. R. Panão, Advances and challenges in explaining fuel spray impingement: How much of single droplet impact research is useful?, Prog. Energ. Combust. **36**, 554 (2010).

[43] N. Laan, K. G. de Bruin, D. Bartolo, C. Josserand, and D. Bonn, Maximum diameter of impacting liquid droplets, Phys. Rev. Appl. **2**, https://doi.org/10.1103/PhysRevApplied.2.044018 (2014).

[44] C. Clanet, C. Béguin, D. Richard, and D. Quéré, Maximal deformation of an impacting drop, J. Fluid Mech. **517**, 199 (2004).

[45] J. M. Gordillo, G. Riboux, and E. S. Quintero, A theory on the spreading of impacting droplets, J. Fluid Mech. **866**, 298 (2019).

[46] R. Rioboo, C. Tropea, and M. Marengo, Outcomes from a drop impact on solid surfaces, Atomization Spray **11**, 155 (2001).

[47] C. Antonini, A. Amirfazli, and M. Marengo, Drop impact and wettability: from hydrophilic to superhydrophobic surfaces, Phys. FLuids **24**, https://doi.org/10.1063/1.4757122 (2012).

[48] K. Koch and R. Grichnik, Influence of surface structure and chemistry on water droplet splashing, Phil. T. R. Soc. A **374**, https://doi.org/10.1098/rsta.2016.0183 (2016).

[49] P. Garcia-Geijo, G. Riboux, and J. M. Gordillo, Inclined impact of drops, J. Fluid Mech. **897**, https://doi.org/10.1017/jfm.2020.373 (2020).

[50] Y. Liu, M. Andrew, J. Li, J. M. Yeomans, and Z. Wang, Symmetry breaking in drop bouncing on curved surfaces, Nat. Commun. https://doi.org/10.1038/ncomms10034 (2015).

[51] W. C. Macklin and G. J. Metaxas, Splashing of drops on liquid layers, J. Appl. Phys. **47**, https://doi.org/10.1063/1.323218 (1976).

[52] E. Berberović, N. P. van Hinsberg, S. Jakirlić, I. V. Roisman, and C. Tropea, Drop impact onto a liquid layer of finite thickness: Dynamics of the cavity evolution, Phys. Rev. E **79**, https://doi.org/10.1103/PhysRevE.79.036306 (2009).

[53] A. M. Worthington, On impact with a liquid surface, Proc. R. Soc. Lond. **34**, 217 (1883).

[54] B. Ray, G. Biswas, and A. Sharma, Regimes during liquid drop impact on a liquid pool, J. Fluid Mech. **768**, 492 (2015).

[55] O. G. Engel, Crater depth in fluid impacts, J. Appl. Phys. **37**, 1798 (1966).

[56] W. Ju, Y. Wu, S. Lin, F. Zhao, and S. Tan, Visual experimental study of droplet impinging on liquid film and analysis of droplet evolution characteristics, Exp. Comput. Multiph. Flow https://doi.org/10.1007/s42757-020-0081-3 (2020).

[57] I. V. Roisman, K. Horvat, and C. Tropea, Spray impact: Rim transverse instability initiating fingering and splash, and description of a secondary spray, Phys. Fluids **18**, https://doi.org/10.1063/1.2364187 (2006).

[58] C. Josserand and S. Thoroddsen, Drop impact on a solid surface, Annu. Rev. Fluid Mech. **48**, 365 (2016).

[59] M. R. Davidson, Spreading of an inviscid drop impacting on a liquid film, Chem. Eng. Sci. **57**, 3639 (2002).

[60] G. Liang, T. Zhang, H. Chen, H. Yu, and S. Shen, Successive impact of multiple droplets on liquid film, Eur. J. Mech. B - Fluids https://doi.org/10.1016/j.euromechflu.2018.09.011 (2018).

[61] D. A. Weiss and A. L. Yarin, Single drop impact onto liquid films: Neck distortion, jetting, tiny bubble entrainment, and crown formation, J. Fluid Mech. **385**, 229 (1999).

[62] T. Gilet, K. Mulleners, J. P. Lecomte, N. Vandewalle, and S. Dorbolo, Critical parameters for the partial coalescence of a droplet, Phys. Rev. E **75**, 036303 (2007).

[63] O. W. Jayaratne and B. J. Mason, The coalescence and bouncing of water drops at an air/water interface, Proc. R. Soc. A **280**, 545 (1964).

[64] A. L. Yarin and D. A. Weiss, Impact of drops on solid surfaces: self-similar capillary waves, and splashing as a new type of kinematic discontinuity, J. Fluid Mech. **283**, 141 (1995).

[65] M. Jalaal, C. Seyfert, and J. H. Snoeijer, Capillary ripples in thin viscous films, J. Fluid Mech. **880**, 430 (2019).

[66] P.-G. D. Gennes, F. Brochard-Wyart, and D. Quéré, *Capillarity and wetting phenomena* (Springer, 2004).

[67] A. N. Chebotarev, K. V. Bevziuk, D. V. Snigur, and Y. R. Bazel, The brilliant blue fcf ion-molecular forms in solutions according to the spectrophotometry data, Russ. J. Phys. Chem. A **91**, 1907 (2017).

[68] M. Taniguchi and J. S. Lindsey, Database of absorption and fluorescence spectra of >300 common compounds for use in photochemcad, Photochem Photobiol **94**, 290 (2018).

[69] P. Gräb and E. Geidel, Spectroscopic studies of food colorings, World J. Chem. Ed. **7**, 136 (2019).

[70] K. K. Varanasi, T. Deng, M. Hsu, and N. Bhate, Hierarchical superhydrophobic surfaces resist water droplet impact, Tech. Proc. NSTI Conf. (2009).

[71] R. Belkofsi, O. Adjaoud, and I. Belabbas, Pressure induced phase transitions and elastic properties of caco3 polymorphs: a density functional theory study, Model. Simul. Mater. Sc. https://doi:10.1088/1361-651X/aacbed (2018).

[72] M. K. Sly, A. S. Thind, R. Mishra, K. M. Flores, and P. Skemer, Low-temperature rheology of calcite, Geophys. J. Int. **221**, 129 (2020).

[73] R. Rioboo, M. Marengo, and C. Tropea, Time evolution of liquid drop impact onto solid, dry surfaces, Exp. Fluids **33**, 112 (2002).

[74] I. V. Roisman and C. Tropea, Impact of a drop onto a wetted wall: description of crown formation and propagation, J. Fluid Mech. **472**, 373 (2002).

[75] C. Josserand and S. Zaleski, Droplet splashing on a thin liquid film, Phys. Fluids **15**, 1650 (2003).

[76] R. Vesipa, C. Camporeale, and L. Ridolfi, Thin-film-induced morphological instabilities over calcite surfaces, Proc. R. Soc. A **471**, https://doi.org/10.1098/rspa.2015.0031 (2015).

[77] I. J. Fairchild and A. Baker, *Speleothem Science: From Process to Past Environments* (Wiley-Blackwell, 2012).

[78] A. J. Baker, D. P. Mattey, and J. U. L. Baldini, Reconstructing modern stalagmite growth from cave monitoring, local meteorology, and experimental measurements of dripwater films, Earth Planet. Sc. Lett. **392**, 239 (2014).

[79] A. Baker, J. C. Hellstrom, B. F. J. Kelly, G. Mariethoz, and V. Trouet, A composite annual-resolution stalagmite record of north atlantic climate over the last three millennia, Sci. Rep. **5**, https://doi.org/10.1038/srep10307 (2015).

[80] S. Verheyden, E. Keppens, Y. Quinif, H. J. Cheng, and L. R. Edwards, Late-glacial and holocene climate reconstruction as inferred from a stalagmite - grotte du père noël, han-sur-lesse, belgium, Geol. Belg. **17**, 83 (2014).

[81] D. Genty and G. Deflandre, Drip flow variations under a stalactite of the père noël cave (belgium). evidence of seasonal variations and air pressure constraints, J. Hydrol. **211**, 208 (1998).

[82] G. A. Ferron and S. C. Soderholm, Esimation of the times for evaporation of pure water droplets and for stabilization of salt solution particles, J. Aerosol. Sci. **21**, 412 (1990).

[83] M. Marengo, C. Antonini, I. V. Roisman, and C. Tropea, Drop collisions with simple and complex surfaces, Current Opinion in Colloid & Interface Science **16**, 292 (2011).